Fe/Co Doped ZIF Derived Nitrogen Doped Nanoporous Carbon as Electrode Material for Supercapacitors

By

Ifra Fiaz Gul

Reg. No. 00000319847

Session 2019-21

Supervised by

Dr. Ghulam Ali

US-Pakistan Center for Advanced Studies in Energy (USPCAS-E)

National University of Sciences and Technology (NUST)

H-12, Islamabad 44000, Pakistan

September 2022

Fe/Co Doped ZIF Derived Nitrogen Doped Nanoporous Carbon as Electrode Material for Supercapacitors

By

Ifra Fiaz Gul

Reg. No. 00000319847

Session 2019-21

Supervised by

Dr. Ghulam Ali

A Thesis Submitted to the US-Pakistan Center for Advanced Studies in Energy in partial fulfillment of the requirements for the degree of MASTER of SCIENCE in Energy Systems Engineering

US-Pakistan Center for Advanced Studies in Energy (USPCAS-E)

National University of Sciences and Technology (NUST)

H-12, Islamabad 44000, Pakistan

September 2022

THESIS ACCEPTANCE CERTIFICATE

Certified that final copy of MS/MPhil thesis written by **Ms. Ifra Fiaz Gul** (Registration No. 00000319847), of US-Pakistan Center for Advanced Studies in Energy (USPCAS-E) has been vetted by undersigned, found complete in all respects as per NUST Statues/Regulations, is within the similarity indices limit and is accepted as partial fulfillment for the award of MS degree. It is further certified that necessary amendments as pointed out by GEC members of the scholar have also been incorporated in the said thesis.

Signature: _____

Name of Supervisor: _____

Date: _____

Signature (HOD): _____

Date: _____

Signature (Dean/Principal): _____

Date: _____

Certificate

This is to certify that work in this thesis has been carried out by **Ms. Ifra Fiaz Gul** and completed under my supervision in Synthesis and Energy Storage laboratory, US-Pakistan Center for Advanced Studies in Energy (USPCAS-E), National University of Sciences and Technology, H-12, Islamabad, Pakistan.

Supervisor: _____
Dr. Ghulam Ali
USPCAS-E
NUST, Islamabad

GEC member 1: _____
Dr. Muhammad Hassan
USPCAS-E
NUST, Islamabad

GEC member 2: _____
Dr. Sehar Shakir
USPCAS-E
NUST, Islamabad

GEC member 3: _____
Dr. Mustafa Anwar
USPCAS-E
NUST, Islamabad

HOD-ESE: _____
Dr. Rabia Liaquat
USPCAS-E
NUST, Islamabad

Dean/Principal: _____
Prof. Dr. Adeel Waqas
USPCAS-E
NUST, Islamabad

Dedication

To my parents, who supported me in every aspect of life and my siblings.

Acknowledgments

First and foremost, I am thankful to Almighty ALLAH who is the creator and author of knowledge. Indeed, without YOUR blessings, this mammoth task would not have been possible. And I acknowledge that without YOUR willingness and guidance, I would not have done a single task. I am grateful to my parents for their unconditional love and sacrifices. your debt for your encouragement, financial and moral support. Thank you for keeping confidence in me.

Dr. Ghulam Ali, I express my sincerest gratitude to you for this opportunity, for your teaching, mentorship, and patience throughout the research. It has been truly a privilege to work with you. I would like to thank my GEC members **Dr. Muhammad Hassan , Dr. Mustafa Anwar,** and **Dr. Sehar Shakir** for their guidance and help throughout my research.

I am also thankful to the staff of Synthesis and Energy Storage Lab specially **Engineer Naveed,** and Advanced energy materials lab engineer **Mr. Asghar Ali** who helped in my research and gave valuable advice during my experimentation. I am also grateful to the other lab staff, faculty members, and administration who were a part of this journey. I profusely thank my husband **Waqas Awan** for his immense support, always being there for me whenever I needed help. Also, all my friends for their support both academically and in general. And to life, an extraordinary experience with so many things to enjoy within a short span. Thank you for giving me so much in the years past, and for more to discover in the years to come.

Abstract

Nanoporous carbon (NPC) for electrochemical energy storage devices has gained much interest due to its high specific area and tunable porosity. Herein, Fe and Co co-doped NPC is synthesized by a simple co-precipitation method followed by carbonization of Fe and Co doped ZIF8 at 900 ℃ (Fe-Co/NPC-900). The structural, morphological, elemental, chemical bonding, surface area, and thermal degradation of the synthesized material have been evaluated using X-ray diffraction, scanning electron microscopy, energy dispersive spectroscopy, X-ray photoelectron spectroscopy, Brunauer–Emmett–Teller method, and thermogravimetric analysis, respectively. The high surface area of 933 m^2 g^{-1} and nanoporous structure of Fe-Co/NPC-900 electrode results in a high specific capacitance of 900 F g^{-1} at a current density of 5 A g^{-1}. The cycle performance of Fe-Co/NPC-900 was remarkable with 88% of the capacitance retention after 5000 cycles at a high current density of 30 A g^{-1}. The high electrochemical performance of Fe-Co/NPC-900 is attributed to the hybrid doping of Fe and Co in nitrogen doped carbon network which offers a synergic effect in reaction.

Keywords: Nanoporous carbon; high specific area; co-precipitation; high specific capacitance; synergic effect.

Table of Contents

List of Figures

List of Tables

List of Publication

Ifra Fiaz Gul, Hirra Anwar, Muhammad Arslan Raza, Rabia Ahmed, Naseem Iqbal, Ghulam Ali

“Fe/Co Doped ZIF Derived Nitrogen Doped Nanoporous Carbon as Electrode Material for Supercapacitors**”**

Journal: **Journal of Industrial & Engineering Chemistry**

Status : **Accepted**

List of Abbreviations

SCs	Supercapacitors
EDLC	Electric double layer capacitance
N	Nitrogen
2mim	2-methyle imidazole
GO	Graphene oxide
rGO	Reduced graphene oxide
ZIF	Zeolitic imidazolate framework
MOF	Metal organic framework
NPC	Nanoporous carbon
MOs	Metal oxides
CNT	Carbon nanotubes
Li-ion	Lithium ion
DMF	Dimethyl formamide
XRD	X ray Diffraction
TGA	Thermogravimetric analysis
SEM	Scanning Electron Microscopy
EIS	Electrochemical impedance spectroscopy
CV	Cyclic voltammetry
CP	Chronopotentiometry
GCD	Galvanic Charge Discharge
C	Capacitance
m	Mass loading
FTIR	Fourier transform infrared spectroscopy
EDS	Energy dispersive X-ray spectroscopy
V	Voltage

Chapter 1: Introduction

1.1 Background

To combat climate change, air pollution, and decreasing fossil fuel supplies, renewable resources are being pursued energetically. To protect the environment and replace fossil fuels, it is more important than ever to have access to green energy production and energy storage systems that work properly. Supercapacitors and batteries have gained considerable significance due to a rapid development in renewable solar and wind energy production. With the increase in the use of electric and hybrid vehicles that emit almost zero CO_2, supercapacitors and batteries are becoming increasingly crucial[1]. Supercapacitors have gained a lot of interest in recent years because they have high power density and cycle life of >100000 cycles [2]. Charge-discharge rates for supercapacitors are rapid, with a simple operating concept. Ragone plot show the relationship between power density and energy density for the most important energy storage systems is shown in Figure 1.1. Both in terms of specific energy and specific power, supercapacitors play a major role and has an important position in the plot. They appear to be the best candidate to meet the growing demands of energy storage devices, as they have a superior power density (superior to lithium batteries and a better energy density (superior to standard capacitors). Supercapacitors already have wide range of applications from consumer electronics, memory back-up systems, industrial power, energy management to public transportation, and military devices. A380 planes' emergency doors were fitted with supercapacitors recently, asserting their safety and reliability.

A typical supercapacitor exhibits high energy density than a conventional dielectric capacitor (5-10 Wh/kg for supercapacitor) but conventional batteries exhibit high energy density than supercapacitors. For example, a conventional lithium ion batterie exhibits specific energy of 120-170 Wh/kg. For uninterrupted energy supply for longer periods of time, combination with batteries (or any other energy source) is however necessary. The energy performance of supercapacitors still has a long way to go before it approaches or surpasses that of batteries.[3]

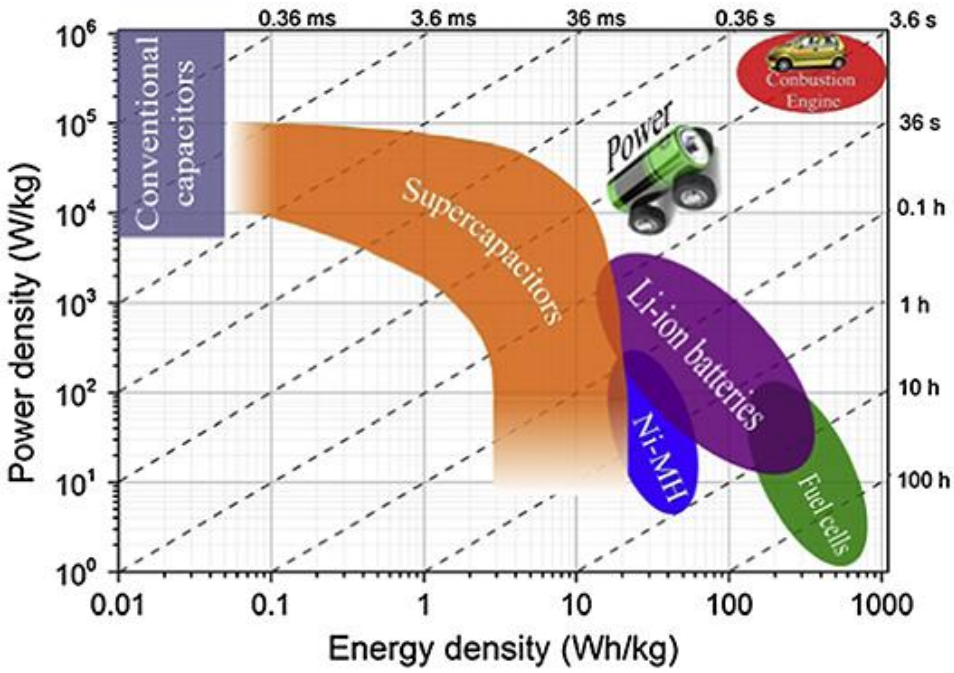

Figure 1-1. Ragone plot showing (Specific energy vs Specific power)[1].

Depending on how they store energy, supercapacitors fall into two categories.

1.1.1 Electrical double layer capacitor (EDLC)

EDLCs have pure electrostatic charge accumulated at the electrode/electrolyte interface as their source of capacitance. Carbon-based materials are most commonly known materials which shows EDLC behavior. Ions in the electrolyte can easily access their large surface area. A typical EDLC have specific energy of 5 Wh/kg which can be sustained for millions of cycles as During charging and discharging, electrodes do not undergo any physical transformation.

1.1.2 Pseudocapacitor

Fast faradic redox reactions are used in pseudocapacitors. Most common electrode materials used in pseudocapacitors are electrically conducting polymers, transition metal oxides, transition metal sulfides and transition metal nitrides. It is possible to superimpose this pseudo-capacitance on top of an electric double-layer capacitance. Their specific energy is better than EDLCs. Due to faradic reactions that cause internal chemical changes in electrodes they exhibit inferior specific power and also short life expectancy. Both

processes can happen at the same time and can produce collaborative influence. But for that to happen type of electrode material is crucial.

1.2 Working of a supercapacitors

Regarding energy storage, they can be divided into two types. One type is EDLC, and the other is Pseudocapcitor. Both types have different working chemistry. In EDLC electrostatic charge is stored at the electrode surface. In Pseudocapcitor faradic reactions happen that contribute towards the pseudo capacitance. For Pseudocapcitor, the main processes for capacitance are reduction, oxidation, and ion intercalation through electrode surface electrodes. Oxidation and reduction occur due to redox active species. In a supercapacitor, these two mechanisms are usually combined. In the following paragraphs, we will discuss in detail the mechanisms of energy storage in supercapacitors.

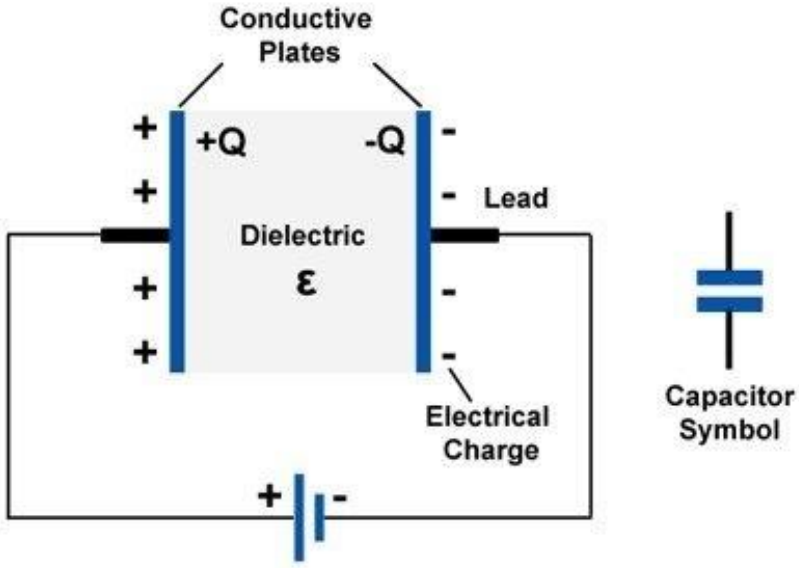

Figure 1-2. Construction of a simple capacitor [2].

In a traditional capacitor, the electric charge is retained in the intensive electric field among two conducting sheets, which are isolated by an insulator. Figure 1.2. As a result of their small plate area and geometrically constrained separation distance, conventional electrostatic capacitors store relatively little energy. Supercapacitors based on the EDL mechanism can store significantly more energy due to the vast interfacial area and atomic

charge split gaps. Helmholtz and Chapman's earlier studies on EDL mode were the basis for Stern's EDL mode development and modification in the 1920s.[4]

Stern mode recognized two distinct ion distribution regions: the inner compact layer, and the outer diffuse layer as shown in Figure 1.3. The electrode strongly adsorbs hydrous ions in compact layer. Specific ions in the interior Helmholtz plane (IHP) and nonspecific counterions in the exterior Helmholtz plane (OHP) comprise the compact layer. As a result of thermal motion in the electrolyte solution, an electrolyte diffuse layer forms around an electrode.

In equation (1) C_{dl} is EDL capacitance, C_H is compact capacitance and C_{diff} is diffusion capacitance.

$$\frac{1}{C_{dl}} = \frac{1}{C_H} + \frac{1}{C_{diff}} \qquad (1)$$

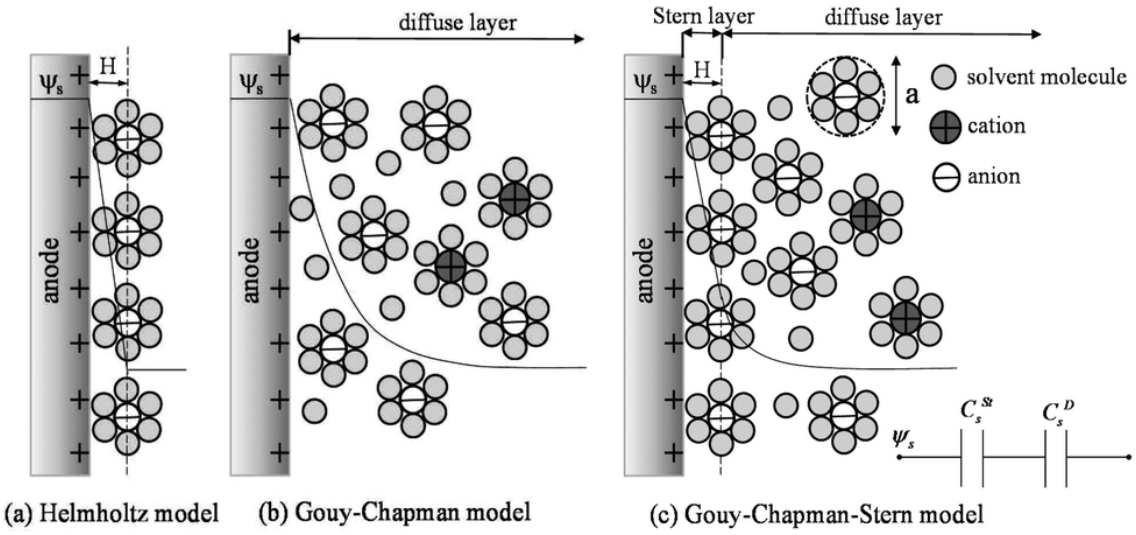

Figure 1-3. Stern model [3].

An electrode surface's EDL behavior hinge on the electrical field around it, the electrode's and electrolyte's inherent characteristics, and the adsorbed ions chemical attraction with the electrode surface, among other factors.

EDLC based on porous electrode material is shown in Figure 1.4, where 2 electrodes in interaction with an electrolyte solution are divided by an insulator. An EDL supercapacitor

is commonly believed to have the same capacitance as a parallel plate capacitor (equation 2).

$$C = \frac{Q}{V} = \frac{\varepsilon_0 \varepsilon_r}{d} A \qquad (2)$$

Where charge on the conductive plates is given by Q, V is the voltage throughout capacitor, A (m^2 g^{-1}) is the area of the conducting electrode and the electrolyte boundary reachable to electrolyte ions, effective thickness of the EDL is represented by d (m) (Debye length), ε_0 = 8.854×10-12 F m^{-1} represents permittivity of vacuum and ε_r is dielectric constant of the electrolyte. High surface area carbon materials usually exhibit EDLC behavior.

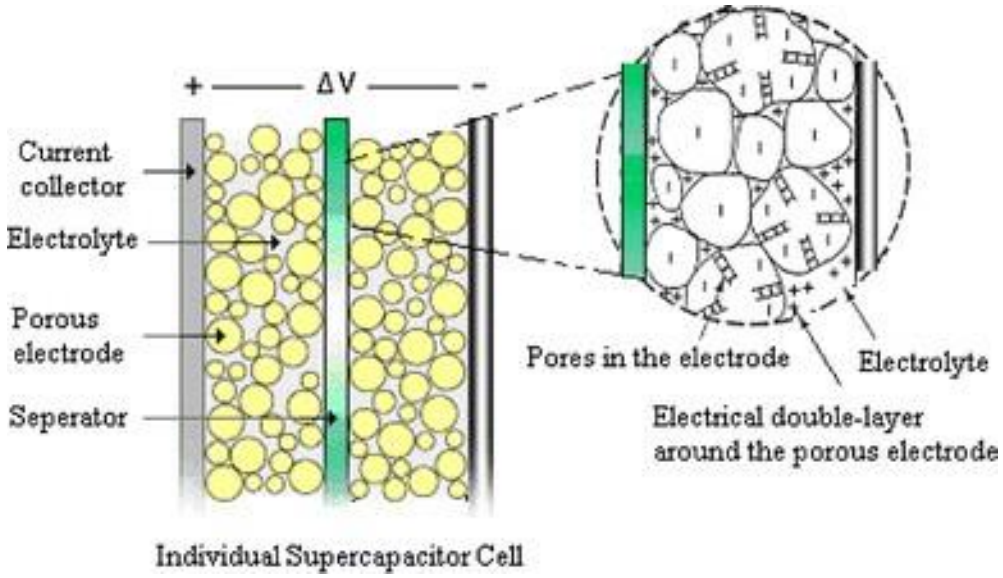

Figure 1-4. Representation of EDLC (high surface area porous electrode is used) [4].

While charging electrons move from external circuit from negative to the positive electrode. Whilst negative ions gravitate to the positive electrode, cations gravitate toward the negative electrode. During the discharging, the reversal processes occur. Between the electrode and electrolyte, there are no charge transfers or ion exchanges, and therefore no ion exchanges or charge transfers occur.

A thermodynamically induced pseudo capacitance differs from the EDL capacitance in that it's related to charge storage Δq and potential change ΔV as follows:

On the electrode materials of a pseudo capacitor, redox faradic reaction transpires, and charge is passed across the electrode/electrolyte interface. A pseudo-faradaic capacitor's processes, on the other hand, are liable to a thermodynamic discrepancy in potential throughout charge buildup, making them more reversible as well as more powerful.[5]

Faradaic processes occur at pseudocapacitive electrodes in three different ways:

- Adsorption of H^+ from the electrolyte that is reversible in nature.
- Ions from the electrolyte are involved in redox reactions.
- Conducting polymer based electrodes with reversible doping and deducing processes [4].

Redox reactions are typically attended by an EDL capacitance part that is relative to the electrochemically comprehensible interface area.

Carbon surfaces with functional groups, organic polymers (Polypyrrole PPy), and transition metal oxides for instance (nickel, iron, manganese) are among the most commonly known active species. When numerous oxidation states from the electrode materials can be attained pseudo capacitors can achieve very elevated energy density. Pseudocapacitors capacitance can be 10 to 100 times superior to EDLC [6]. But sluggish faradic reactions and morphological adjustments during the operation precedes to lower specific power and life expectancy is also diminished.

1.3 Supercapacitors Evaluation

The supercapacitor has a similar structure to a battery. Both electrodes are in interaction with an electrolyte solution are divided by an insulator in a single-cell supercapacitor, as shown in Figure 1.4. All of the cell's components are similar to two simple capacitors attached in series. An individual supercapacitor's equivalent resistor and capacitor (RC) circuit is shown below Figure 1.5. C_a and C_c represent anodic and cathodic capacitances, respectively. Cellular equivalent series resistance (ESR) is represented by the number R_s. R_F is the self-discharge resistance of a single electrode. This equation (3) is employed to evaluate the total capacitance (C_T) of the entire cell. In this case, the supercapacitor is depicted as symmetric supercapacitor because the overall capacitance (C_T) is half of whichever single electrode's capacitance.

$$\frac{1}{C_T} = \frac{1}{C_a} + \frac{1}{C_c} \tag{3}$$

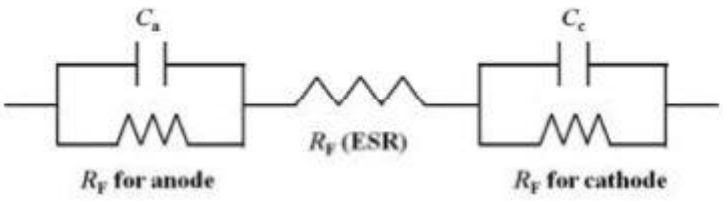

Figure 1-5. Resistor-capacitor (RC) equivalent circuit for supercapacitor [5].

Where material of both electrode is different, C_a is not equal to C_c, then it is discussed to as an asymmetries supercapacitor (ASC). One with smaller capacitance dominates C_T [7]. Overall, electrode material has a significant impact on capacitance and stored charge.

For a single-cell supercapacitor, E represents the energy collected and P represents specific power, can be expressed as equations (4) and (5):

$$E = \frac{1}{2} C_T V^2 \tag{4}$$

$$P = \frac{V^2}{4R_s} \tag{5}$$

Where the cell voltage (V), the cell capacitance (F), and the electrode surface resistance (ESR) (ohms).

From the following equations, it is evident that for the final performance of the supercapacitor, V, C_T, and R_s are critical constraints to be aware of. The electrolyte solution's thermodynamic stability determines the cell's voltage, which is dependent on the electrode materials. Electric field strength (ESR) is determined by a number of factors, including electrode matrix and electrolyte solution intrinsic electronic properties, as well as ions' mass transfer resistance and interaction resistance between the current collecting plate and electrode. It is necessary to increase the capacitance of both electrodes to maximize the whole cell capacity. For a supercapacitor to perform well, it must have a high capacitance value, a high operating cell voltage, and a low ESR. Further development

and more research is a need to synthesize new superior electrode materials to elevate aggregate performance of supercapacitors [2].

A three-electrode electrochemical cell (beaker cell) shown in Figure 1.6. Beaker cell is used to test the electrochemical performance of a material at lab scale. Beaker cell has a working electrode which has the material that is being tested for performance. A reference electrode with respect to which potential is applied and measured. Counter electrodes assist in the application of potential and complete the circuit so that current can pass through. The specific capacitance of a single electrode is calculated from a three-electrode cell configuration.[8]

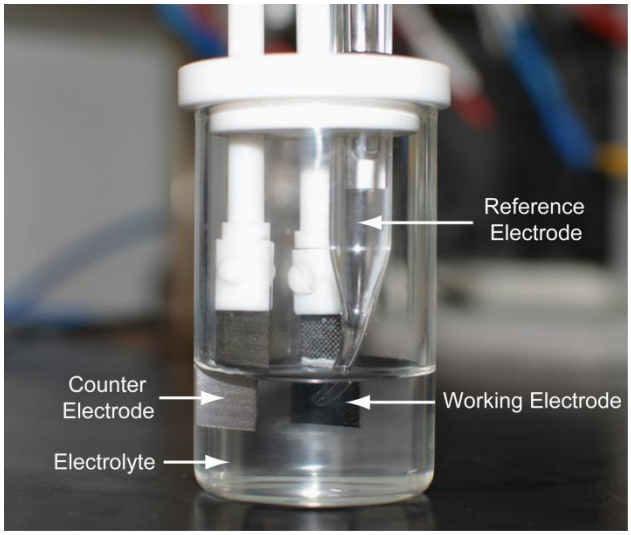

Figure 1-6. A three-electrode Beaker cell [6].

As a packaged supercapacitor cell's performance is closely matched by a two-electrode test fixture, the electrochemical activity can be more accurately assessed. They can be purchased commercially or made from two stainless steel plates. A three-electrode cell allows just working electrode to be analyzed, whereas a two-electrode configuration allows to analyze both electrodes separately.

Importantly in three-electrode cell, the applied potential on working electrode is given according to reference electrode used and is applied totally on working electrode. Electric potential applied to the system are distributed equally to every electrode in a two-electrode cell. Accordingly, the working electrode in 3-electrode cell is subjected to two times the potential range as that of a 2-electrode cell, which results in a doubled capacitance

calculation. In two electrode cell, when the RE and WE are in close proximity, the RE has the ability to accurately control the interfacial potential. These parameters are used at the packaged cell level to evaluate supercapacitor performance [9].

1.4 Problem Statement

MOF-based materials are potentially attractive for electrochemical devices due to their large effective surface area, high porosity, and numerous redox reaction sites. Pure MOFs have two primary disadvantages: low conductivity and particulate aggregation. As a result, supercapacitors have low energy density (>50Wh/kg) as compared to batteries(30-300Wh/kg) that limits the MOFs as electrode material and their cyclic stability is also a serious concern.

1.5 Objectives

The objective of this research was to fabricate the highly porous electrode material with high specific surface area. The physiochemical properties were studied by X-ray diffraction (XRD), Scanning electron microscopy (SEM), X-ray photoelectron spectroscopy (XPS) and electrochemical properties were studied by electrochemical impedance spectroscopy (EIS), cyclic voltammetry (CV) and galvanostatic charge discharge(GCD).Micropores can increase the active surface area of electrode materials, thereby influencing electrode capacitance . The specific capacity of a carbon-based supercapacitor is influenced by the surface region and the presence of defects.

Summary

This chapter discuss the background and comparison of all energy storage systems and compare them to supercapacitors. Further chapter 1 discusses the types and working of supercapacitors and their performance parameters in detail.

List of References

[1] P. Simon, Y. Gogotsi, Materials for electrochemical capacitors, Nat. Mater. 7 (2008) 845–854. https://doi.org/10.1038/nmat2297.

[2] L. Zhang, X.S. Zhao, Carbon-based materials as supercapacitor electrodes, Chem. Soc. Rev. 38 (2009) 2520–2531. https://doi.org/10.1039/b813846j.

[3] A. Ghosh, Y.H. Lee, Carbon-based electrochemical capacitors, ChemSusChem. 5 (2012) 480–499. https://doi.org/10.1002/cssc.201100645.

[4] B.E. Conway, V. Birss, J. Wojtowicz, The role and utilization of pseudocapacitance for energy storage by supercapacitors, J. Power Sources. 66 (1997) 1–14. https://doi.org/10.1016/S0378-7753(96)02474-3.

[5] X. Zhao, B.M. Sánchez, P.J. Dobson, P.S. Grant, The role of nanomaterials in redox-based supercapacitors for next generation energy storage devices, Nanoscale. 3 (2011) 839–855. https://doi.org/10.1039/c0nr00594k.

[6] B.E. Conway, Energetics and Elements of the Kinetics of Electrode Processes, Electrochem. Supercapacitors. (1999) 33–65. https://doi.org/10.1007/978-1-4757-3058-6_3.

[7] G. Wang, L. Zhang, J. Zhang, A review of electrode materials for electrochemical supercapacitors, Chem. Soc. Rev. 41 (2012) 797–828. https://doi.org/10.1039/c1cs15060j.

[8] M.D. Stoller, R.S. Ruoff, Best practice methods for determining an electrode material's performance for ultracapacitors, Energy Environ. Sci. 3 (2010) 1294–1301. https://doi.org/10.1039/c0ee00074d.

[9] M.D. Stoller, S. Park, Z. Yanwu, J. An, R.S. Ruoff, Graphene-Based ultracapacitors, Nano Lett. 8 (2008) 3498–3502. https://doi.org/10.1021/nl802558y.

[10] B. Diouf and R. Pode, "Potential of lithium-ion batteries in renewable energy," *Renew. Energy*, vol. 76, pp. 375–380, 2015, doi: 10.1016/j.renene.2014.11.058.

[11] F. Jia, K. Soucie, S. Alisat, D. Curtin, and M. Pratt, "Are environmental issues

moral issues? Moral identity in relation to protecting the natural world," *J. Environ. Psychol.*, vol. 52, pp. 104–113, 2017, doi: 10.1016/j.jenvp.2017.06.004.

[12] X. Tang, W. Yang, X. Hu, and D. Zhang, "A novel simplified model for torsional vibration analysis of a series-parallel hybrid electric vehicle," *Mech. Syst. Signal Process.*, vol. 85, pp. 329–338, 2017, doi: 10.1016/j.ymssp.2016.08.020.

[13] T. H. Kim, J. S. Park, S. K. Chang, S. Choi, J. H. Ryu, and H. K. Song, "The current move of lithium ion batteries towards the next phase," *Adv. Energy Mater.*, vol. 2, no. 7, pp. 860–872, 2012, doi: 10.1002/aenm.201200028.

[14] Y. Sun, "Lithium ion conducting membranes for lithium-air batteries," *Nano Energy*, vol. 2, no. 5, pp. 801–816, 2013, doi: 10.1016/j.nanoen.2013.02.003.

[15] J. Scheers, S. Fantini, and P. Johansson, "A review of electrolytes for lithium-sulphur batteries," *J. Power Sources*, vol. 255, pp. 204–218, 2014, doi: 10.1016/j.jpowsour.2014.01.023.

[16] T. Kojima, T. Ishizu, T. Horiba, and M. Yoshikawa, "Development of lithium-ion battery for fuel cell hybrid electric vehicle application," *J. Power Sources*, vol. 189, no. 1, pp. 859–863, 2009, doi: 10.1016/j.jpowsour.2008.10.082.

[17] G. E. Blomgren, "The Development and Future of Lithium Ion Batteries," *J. Electrochem. Soc.*, vol. 164, no. 1, pp. A5019–A5025, 2017, doi: 10.1149/2.0251701jes.

[18] M. Armand *et al.*, "Lithium-ion batteries – Current state of the art and anticipated developments," *J. Power Sources*, vol. 479, no. June, 2020, doi: 10.1016/j.jpowsour.2020.228708.

Chapter 2: Literature Review

2.1 Electrode Materials

The electrode material used can also alter the electrochemical presentation of a supercapacitor. As a result, most electrode materials excel in only one of these areas - mechanical strength or electrochemical performance. There are common qualifications and strategies for selecting electrode materials in both storage mechanisms described.

Supercapacitors' capacitance and charge storage are highly dependent on the materials used for the electrodes. Improve the current electrode materials' performance by developing new materials with greater capability and functionality. A large electrode surface area is critical to the supercapacitor's capacitance. Surface area increases do not result in a linear shift in capacitance measurements as the absolute surface area cannot be accessed when a material goes into interaction with an electrolyte [1]. It may be more accurate to describe electrochemically active surface areas than electrode capacitance in certain cases. When it comes to electroactive surface area, the electrode material's porosity plays a crucial role. According to Largeot et al., the electrode materials that produced extreme double-layer capacitance had pores that were either bigger or tinier than the electrolyte ion size, causing a considerable decline in capacitance. However, an expansion in pore size surges the average gap between the inside of the ion and the pore wall, that declines the overall capacitance of electrode with bigger pores. Pore size and distribution for a particular surface area of the electrode used are vital elements in determining the porosity linked with the fabrication of high-capacity electrodes [2]. Consequently, capacitance is highly dependent on the electrode's reachable electrolyte surface area. It is common to classify materials used in electrodes into three major categories:

- Transition metal oxides
- Carbon-based materials
- Organic polymers

Dur to the large surface area of carbon materials, they have improved interaction with the electrolyte hereby increasing the surface charge and enhancing the overall capacitance of electrode [3]. Charge transfer reactions can be made more efficient by developing porous

structures at micro and nano scale as they increase diffusion rate by offering additional electroactive sites [4].

Metal organic frameworks (MOFs), a class of complexes known as porous-coordination-polymers (PCPs). They have metal ions that are connected to an organic linkers to form multi-dimensional assemblies [4,5]. MOF possess a unique set of properties due to which they can be used to fabricate nano or even hollow structures. For example, there is a lot of work happened in past few years on ZIF-67 which is a MOF to form core shell hollow structure. Core shell structures have a hollow shell and inner pores. MOF gathered much attention due to the fact that they have very large surface areas, also their porosity can be tuned by changing the synthesis conditions like temperature and pressure [6]. Their morphology is also flexible and can be molded according to the requirement by playing with the process conditions. It is important to note that different research groups contribute significantly to the synchronized advancement of MOFs at the nano and microscale levels [7].

2.2 Carbon based composites

Carbon based materials have unique structure and there is a lot of research going on carbon-based electrodes. As a result, they are difficult to manufacture. Nanocarbons can be mixed to create electrodes with high capacity. A practical application of nanotechnology may also be too far away. Even when tested at lab scale, nanomaterials that perform well with low electrode loading may not work well with electrodes that have a high electrode loading in practical applications. Incorporation of nanostructures on to the carbon surfaces can be a solution they are mechanically stable. They can be used as strong template. Mesoporous structures can be formed by embedding nanocarbons such as graphene or nanotubes. In order for SC to work, the electrode material's porosity must be maximized [8].

2.2.1 Carbon nano tubes (CNTs)

CNTs are synthesized as a result of sp2 hybridization, graphene sheets are wrapped in covalently bonded carbon atoms. In terms of single-walled CNTs (SWCNTs) and porosity, graphene sheets are classified by the number of layers and porosity. That deliver mechanical potency and conductivity to the complex material. After 50,000 cycles in

aqueous electrolyte solutions, supercapacitor electrode that has CNT dopped composite showed negligible capacitance fading. Same system without using CNTs couldn't compete with it and exhibits a decline in capacitance after 30,000 cycles. (Figure 2.1) [9]. Compared to CNTs combined with GQDs, these composites produced better results (200 mF/cm^2 vs 0.44 mF/cm^2). Graphene, despite its intriguing properties, is still a long way from being used as electrodes in practical energy storage devices, as this study shows.

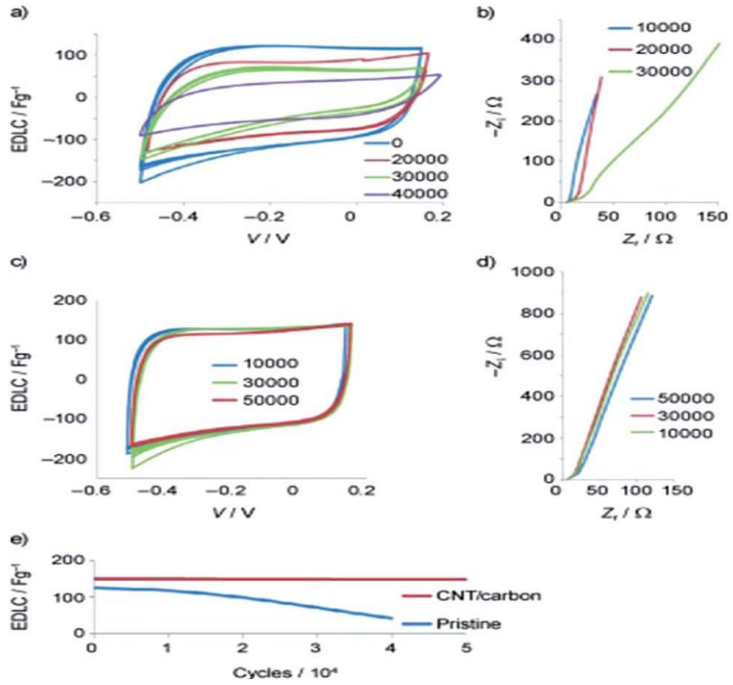

Figure 2-1. (a, b) Cyclic voltammetry and Nyquist plot of carbon-based polymer electrodesin 6M KOH electrolyte (c, d) Carbon based polymer electrode with CNTs 1.5 wt. %. (e) Capacity vs. cycle number plot [1].

CNTs dopped polymers also exhibit a similar example. 170 F/g capacitance was measured in a voltage ranging from 0 V - 2.5 V at a current density of 118 mA g^{-1} while organic electrolyte was used. We measured a capacitance decay rate of less than 7 percent over a period of 10 000 cycles [9].

Composite materials containing CNTs, and graphene have also been tested for SC applications. Their synthesis was rather complex. Due to the low performance of the composite materials, the authors must explain why combining these two jointly as electrode is beneficial. Uniformity of pore size distribution in CNTs complex composites can now be made using an entirely new fabrication technique. As a template, CNTs and

polystyrene beads were electrochemically co-decomposed. After that electro polymerization is achieved. Finally, pyrolysis is done after the template extraction. Surface area of the synthesized composite is 5 times greater than the simple CNTs. A uniform pore size distribution on CNT–carbon composites increased the arial capacitance of lowest 6 mF/cm^2 to 200 mF/cm^2 (Figure 2.2) [10]. Comparison of this study's results with electrodes that did not contain nanoparticles shows that tough carbonaceous templates are necessary to support nanocarbons.

Because CNT composites have hierarchical structures, they may have better electrochemical performance, allowing the development of high-power supercapacitors. CNTs grown directly on carbon nanofiber (VCNTs/CNFs) using a vertically aligned CNT synthesizing method exhibit impressive capacitance performance. It was found that VCNT/CNF supercapacitors assembled in ionic liquid solution could achieve a gravimetric energy of 70 Wh/kg at the current density of 0.5 A/g at the temperature of 30 ºC. After testing it for more than 20,000 cycles, the capacitance was only reduced by 3 percent, according to the study [11]. It has been pointed out that articulating the specific energy density of supercapacitors in terms of the electrode mass loading is misleading, since electrolyte solution weight can be much higher than electrode weight.

2.2.2 N-doped carbons

Alterations in the physiochemical, and electrochemical characteristics of carbonaceous materials can be caused by nitrogen doping carbon. Nitric acid can also modify the electronic and crystallographic arrangement of carbons to increase chemical stability as well as it enhances electrical conduction. In addition to supercapacitors and catalysis, nitrogen-doped carbons are also used in adsorption and separation processes [13].

Most Nitrogen doped carbon materials are synthesized using N-containing precursors [14]. Nitrogen matter in common precursors is a limiting factor in this type of synthesis. As a result of an effort to raise the nitrogen quantity in the precursors, the mesostructured of the carbons degrades. It was recently reported that carbonization, nitrogen functionalization, and activation can all be combined into one process to synthesize N-doped materials [15].

N-doped carbon materials can have a very higher surface area of 1400 m^2/g. Compared to carbon materials without nitrogen, these materials have a higher capacitance (6.8 mF cm-

2) and a lower ion diffusion resistance. Simple carbon materials without N-doping can have a high capacitance 6.8 mF/g and have smaller diffusion resistance [16].

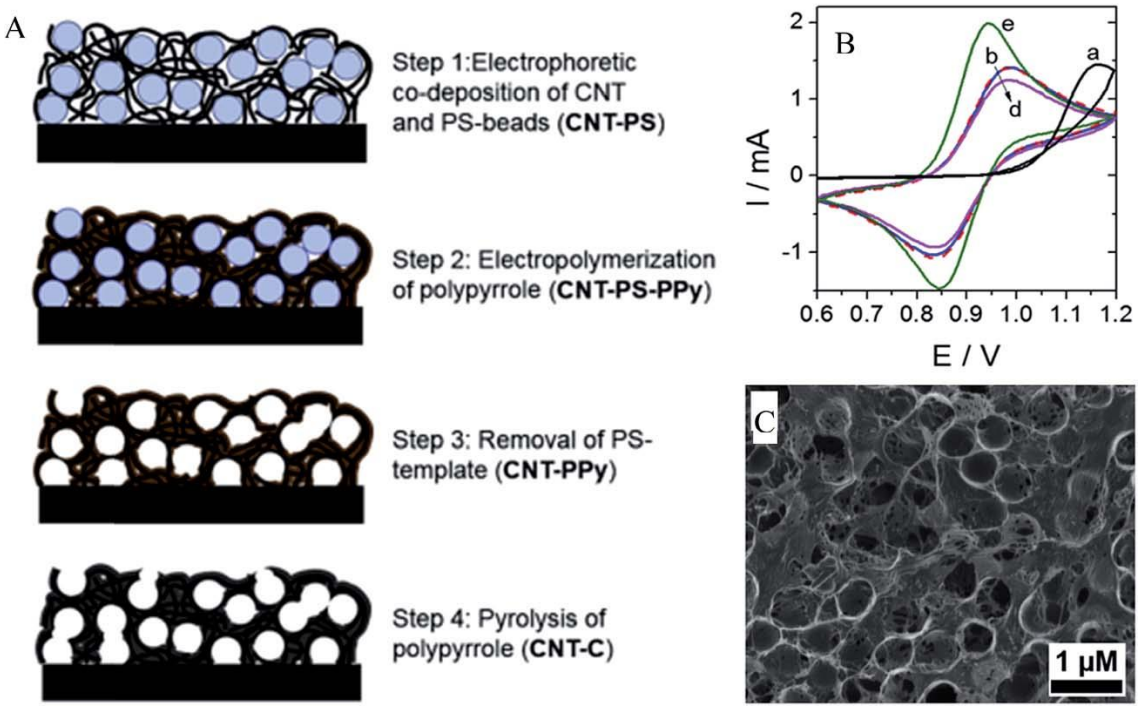

Figure 2-2. (A) Schematic of synthesis of CNT–C (B)CV profiles in 0.15 M H_2SO_4 electrolyte (a) Glassy carbon (b, e, d) CNTs 1,2,3 CNT layers (e) macroporous CNTs in 3M H_2SO_4 at sweep rate of 10 mV/s (C) SEM image of CNTs) [12].

Smaller, highly monodispersed particles can improve EDLC performance and reduce charge transfer. As a result of the electrolyte solution's accessibility of the pores, composites containing N-doped carbon and carbon spheres can lead to superior capacitance. Researchers used solgel method to synthesize N-dopped polymeric spheres. Their capacitance was 390 F/g and their current density was 1 A/g, and they retained their capacity of about 98 percent after 8000 cycles [17]. A nitrogen-rich carbon source is used as a precursor in this process. By using this method, complex assembly processes are eliminated, and the template is uniformly filled with the heteroatom source. 260 F/g of capacitance can be obtained using these materials as supercapacitor electrodes at a current density of 20 mA/g. On the practical side of things, N-doped AC electrodes are extremely valuable, as they can improve specific capacity and mass loading, comparatively simple fabrication from profuse precursors [18].

2.2.3 Graphene composites

Two-dimensional graphene sheets are composed of carbon atoms that are connected by hexagonal networks. Graphene sheets have many advantages over other materials. In contrast, the oxidation produces' adsorption shrinks the surface area of the oxidized graphene sheets by stacking them back up again. Further activation is required to separate the graphene sheets from each other and their surface area is enhanced [19]. As a result of high-temperature annealing, the sheets of graphene-oxide can become separated. GO/AC composites were synthesized in one step in a recent study. An eight-fold increase in surface area was observed after the composite material had been annealed. Graphene's electrochemical performance also improves, compared to graphene without active carbon [20]. It is possible to create mesopores between microporous scaffolds by assembling graphene plates in a porous arrangement and taking advantage of graphene's large surface area. Due to this increased diffusion efficiency, the electrochemical performance is enhanced as well. Electrodes made from this composite had a three-fold higher energy density than electrodes made from pristine activated carbon.

The honeycomb-like lattice of carbon atoms in graphene makes it an exceptional matrix for the preparation of 2D porous materials. Porous organic materials are often assembled using Schiff-base chemistry. Supercapacitors with capacitances of 430 F/g at current density 0.1 A/g were made using TPP as a precursor [21].

A new arrangements of hollow carbon atoms in way that they are curved to form a curved sheet like assembly should be discussed. A curvature in the particle's morphology prevents the particles from stacking. Using silica atoms with a sturdy core and a matrix with N-rich precursor can be used to create these carbon capsules by nano casting. (Figure 2.3). These carbon capsules have a high performance in an aqueous medium, with an efficiency of 240 F/g and capacitance is retained by 72 percent after 10,000 cycles. With a current density of 100 A g^{-1} and a capacitance retention of 93 percent after 10000 cycles, these supercapacitors perform better in an organic medium [22]. For supercapacitor electrodes, carbon-only materials have been studied for years. In addition, graphene and CNTs have a large surface area that could lead to the maximum specific EDL capacitance. These materials alone, however, present engineering challenges and produce a modest volumetric capacitance when used in practical cells.

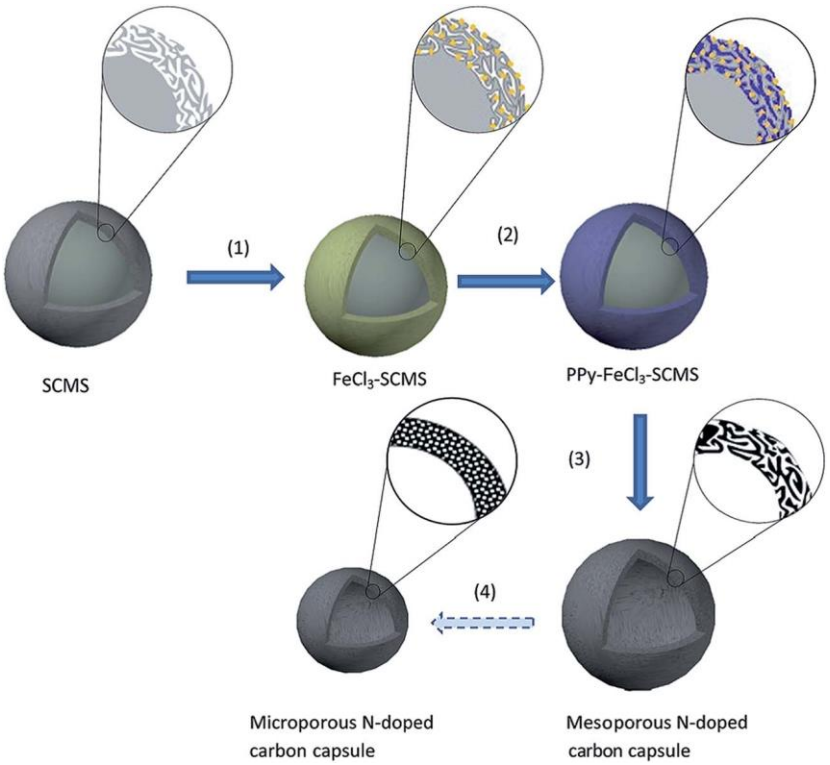

Figure 2-3. Synthesis of Carbon capsule [15].

Coupled composite structures combining different types of carbon have made great strides in the area. In addition to making practical electrodes, using such composite materials could pave the way for the fabrication of porous structures with improved properties. In some cases, carbon-based composite electrodes had capacitances that were almost double than those of carbon electrodes that were left unmodified. CNT-activated carbon composites are a great example of such an improvement and advantage. CNTs have been mixed with electrode materials for a long time.

Nanofabrication methods, which allow materials to be controlled at atomic scale, and the ability to mass produce nanomaterials are promoting and advancing these approaches.

2.3 Metal-oxide composites

Supercapacitors and hybrid devices have extensively investigated a variety of metal oxides, including $Ru_2 O_3$, $V_2 O_5$, $Fe_3 O_4$, $Co_3 O_4$, $Ni_2 O_3$, and $Ti_2 O_2$. When compared to carbon materials' capacitive charge storage mechanism (EDL), metal oxides demonstrate pseudocapacitance. Activated carbon electrodes can be combined with other oxides (Co_3O_4, NiO, TiO_2) to form battery-type electrodes. In all of these oxides, the multivalent

nature of their transition metals is responsible for their redox behavior. Protons and/or hydroxide anions interact well with most of these oxides because their oxidation states changes, and they occur reversible oxidation and reduction reactions that result affect both the electrode surface and the bulk of these oxides.

Most metal oxides suffer from excellent specific capacitance or capacity because they have low conductivity. All of these aspects are excellent in carbon materials, which have a relatively low specific capacitance. A composite electrode with a conductive backbone that supports nanocomponents with high capacitance/capacity may be created by integrating nano metal oxides with carbon structures.

2.3.1 MnO_2-based composites

Compared to other transition-metal oxides, MnO_2-based electrodes are gaining in popularity for energy storage applications. It is generally used in aqueous solutions as a pseudocapacitive charge-storage medium where only the thin top layer of MnO_2 is active and involved in the redox reaction. However, due to their low conductivity, MnO_2 may suffer with reduced capacitance and specific power.

This research has focused on many carbon substrates, including carbon black (standard), activated carbon (carbon nanofibers), graphene, micro fibrous carbon paper (micro fibrous carbon paper), carbon aerogels, and microporous carbon surfaces. MnO_2 and carbon composites are also synthesized by the researchers by the following techniques. Yan synthesized a CNT-MnO_2 composite. This composite gave specific capacitance of 950 F/g. Yan's multi-wall CNT–MnO_2 composite, synthesized by microwave irradiation, gave one of the best results ever reported. It has a capacitance retention of 95 percent after 500 cycles [23].

MnO_2 composite electrodes were also supported by graphene. Composite materials can be synthesized in a variety of ways to achieve high specific capacitances of 520 F/g and excellent cycle life [24]. It has been possible to make MnO_2–graphene composites, for example, by microwave-induced process of MnO_2 nano particles deposited on graphene sheets. In comparison to graphene or burnside-type MnO_2, this composition exhibits a capacitance of 310 F/g. Furthermore, only five percent capacitance was reduced after 15000 cycles. As a result of the graphene network's increased conductivity and surface area, their superb electrochemical activity was ascribed to this. A composite electrode

based on MnO_2 with graphene and CNTs has superior electrochemical performance when contrasted to electrodes made from their individual components, according to this research [25].

2.3.2 RuO_2-based composites

RuO_2 is considered to have the best pseudo capacity of all. On the surface of RuO_2 particles, protons are electrostatically adsorbed, resulting in a pseudocapacitive reaction. To compensate for the high cost, electrodes must be designed to maximize capacitance with the least amount of metal oxide [26]. Composite materials hold the key to finding a solution. RuO_2 composites with carbon have great promise in electronic industry. Surface RuO_2 coating on porous electrodes is the focus of research in this field. RuO_2–CNT composites were prepared by atomic layer deposition (ALD) on porous carbon nanotubes. After that oxidation was done. Electrode design for energy storage devices benefits from this technique's tremendous homogeneity, precise thickness management, and ability to deposit on large surface areas (Figure 2.4) [27].

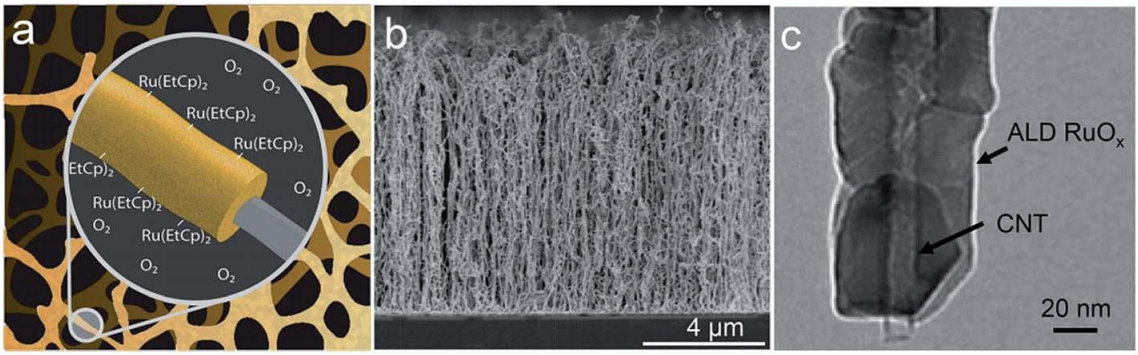

Figure 2-4. (a) RuO_x deposition on porous electrode Ru $(EtCp)_2$ and oxygen are pulsed sequentially to achieve monolayer deposition. (b) SEM image of ALD/RuO_x coated vertical alligned CNTs (c) TEM image of a ALD/RuO_x coated CNT [28].

According to several publications, RuOx–CNTs have a specific capacitance of 650 F/g and its specific power is 17 kW/kg [29]. Figure 2.5 shows RuO_2/Graphene as another example. RuO_2 particles can be deposited onto graphene sheets to create other interesting composites. Graphene sheets have higher energy densities, but RuO_2 as a single active electrode material has lower energy densities. As a result, such composite electrodes have elevated specific energy of 7.2 Wh/kg. These electrodes also have tremendous cycle life,

as well. Electrodes made from RuO_2 and graphene are shown in Figure 2.5, along with some representative data [30].

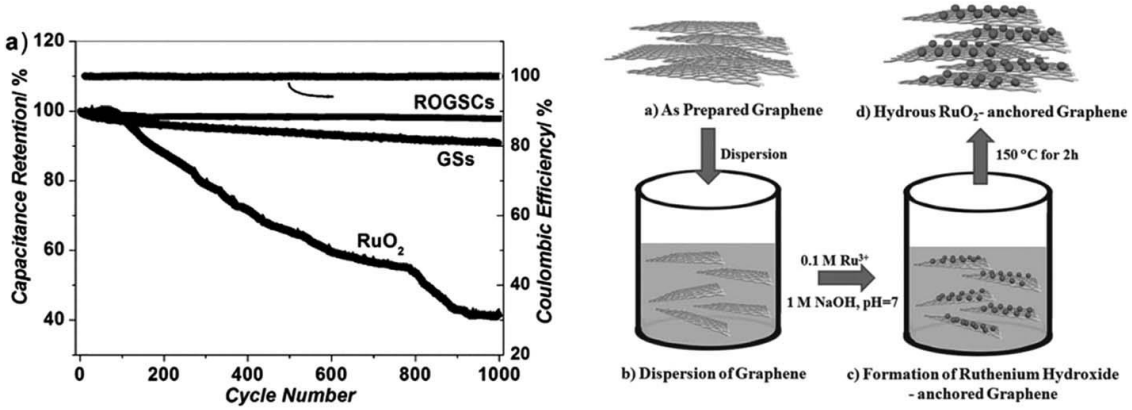

Figure 2-5. (a) cyclic stability and columbic efficiency of graphene sheets, RuO_2 and RuO_2/graphene (b,c) Synthesis process of RuO_2/graphene sheets composite.

2.3.3Fe_3O_4- and V_2O_5-based composites

A magnetite-carbon composite electrode was examined. 220 F/g specific capacitance is observed in these electrode composites, which have good cyclability. An electrode for a supercapacitor made of Fe_3O_4 and CNTs was reported in literature. Using hydrothermal process, the CNT–Fe_3O_4 composite material was created. In terms of specific capacitance, the electrode measured at 117 F/g, and the electrode's specific energy was 16 Wh/kg [31]. Fe_3O_4–RGO performed better electrochemically than CNTs in a similar method. Fe_3O_4–RGO composite give a capacity of 220 F/g after 3000 cycles. It has also been possible to prepare Fe_3O_4-RGO nanocomposites by using benzyl alcohol [32]. As a result of a greater iron content in the precursor, the RGO surface is completely covered by FeO_x particles, resulting in a densely stacked sheet that doesn't restack when dry.

Crystal structure and faradic activity of V_2O_5 are well-known characteristics of this material However, due to its poor conductivity, it is unable to perform electrochemically. Studies prove that V_2O_5–RGO composite performs tremendously in aqueous electrolyte. Their specific capacitance approaches 550 F/g, and their specific power approaches 500 W/kg. This section can be summarized as follows: The carbonaceous components of the composite materials provide an electronically interconnected backbone that enhances the specific capacitance and metal oxides cycle stability [33].

2.3.4 NiO-based composites

Activated carbon-Ni $(OH)_2$ hybrid cells can use NiO-carbon composites as a positive electrode. When nickel oxide in alkaline solution undergoes a redox reaction, the equation [34].

$$NiO + OH^- \leftrightarrow NiOOH + e^-$$

This is because the usual CV profiles of these materials cannot be used to calculate capacitance, which is why most literature is reported in F/g units. A wide electrochemical window must be used to convert all reported capacities from F/g to mAh/g units. Three-dimensional (3D-RGNiO) nanoparticle composites were studied for their electrochemical behavior as battery electrode materials. It was made in 3 steps, which included the of NiO nanoparticles adsorption on the graphene and thermal treatment to decorate it. The 3D-RGNi composite has a higher specific capacity than the RGNiO composite and the 3D-RG composite. Aside from its good cycling stability, this composite electrode material has an 87 percent capacity retention after 2000 cycles. Large surface area and fast reaction kinetics were attributed to the porous structure of the graphene network [35].

Batteries with active materials based on carbon nanotubes or carbon nanofoam can also be implemented in supercapacitors. Using a one-step solvothermal process, a NiO nanoparticles composite on the surface of RG and CNTs was reported. More than twice as much specific capacity as pure NiO is delivered by this ternary composite in an electrolyte containing 6 M KOH, and it retains 94% of its capacity after 1000 cycles [36].

2.4 Metal–organic frameworks

The MOFs are multi-dimensional materials composed of metal centers connected by organic linkers. There may be several thousand square meters per gramme of surface area in some of these MOFs because of the development of void spaces within the coordination network of the organic molecules. They are, however, not widely used in electrochemical systems because of their non-conducting nature. We've already discussed the advantages of composite materials that combine both electrochemical and redox-active materials with conducting carbons. Fleker et al. synthesized MOF-activated carbon compositions to talk about nonconductive nature of MOFs, a result of the network's coordinating bonds. MOF nanoparticles in contact with activated carbon show an interesting EPR signal [37]. The

MOF's Cu^{2+}/Cu^{+} redox couple increases the AC's double-layer capacitance by 30 percent. Yaghi et al. conducted a comprehensive study on the growth of MOF on graphene sets. Zirconium-MOF showed an aerial capacitance of 5.09 μF/cm for over 10,000 charge/discharge cycles [38].

Better composite materials may be produced by using wet or dry nanofabrication techniques. As organic nanoparticle fabrication techniques have become more homogeneous and reproducible, they have transformed the pharmaceutical and medical industry. For complex composite materials, the rapid prototyping field opens up new possibilities. Of course, each technique must be adapted to fabricate high surface area electrodes, which requires additional development.

Summary

This chapter consists of the literature review on the types of electrode materials used for supercapacitor application. In addition, the performance of the electrode materials is also discussed in the chapter. Moreover, this chapter also contains the benefits and shortcomings of various MOF derived materials for the energy storage applications.

List of References

[1] E. Frackowiak, S. Delpeux, K. Jurewicz, K. Szostak, D. Cazorla-Amoros, F. Béguin, Enhanced capacitance of carbon nanotubes through chemical activation, Chem. Phys. Lett. 361 (2002) 35–41. https://doi.org/10.1016/S0009-2614(02)00684-X.

[2] W. Li, N. Islam, S. Azam, Z. Xu, J. Warzywoda, Z. Fan, ZIF-67-derived edge-oriented graphene clusters coupled with carbon nanotubes containing encapsulated Co nanoparticles for high-frequency electrochemical capacitors, Sustain. Energy Fuels. 3 (2019) 3029–3037. https://doi.org/10.1039/c9se00503j.

[3] Z. Chen, V. Augustyn, J. Wen, Y. Zhang, M. Shen, B. Dunn, Y. Lu, High-performance supercapacitors based on intertwined CNT/V 2O 5 nanowire nanocomposites, Adv. Mater. 23 (2011) 791–795. https://doi.org/10.1002/adma.201003658.

[4] L. Wan, E. Shamsaei, C.D. Easton, D. Yu, Y. Liang, X. Chen, Z. Abbasi, A. Akbari, X. Zhang, H. Wang, ZIF-8 derived nitrogen-doped porous carbon/carbon nanotube composite for high-performance supercapacitor, Carbon N. Y. 121 (2017) 330–336. https://doi.org/10.1016/j.carbon.2017.06.017.

[5] M. Jiang, X. Cao, D. Zhu, Y. Duan, J. Zhang, Hierarchically Porous N-doped Carbon Derived from ZIF-8 Nanocomposites for Electrochemical Applications, Electrochim. Acta. C (2016) 699–707. https://doi.org/10.1016/J.ELECTACTA.2016.02.094.

[6] G. Zhang, X. Xiao, B. Li, P. Gu, H. Xue, H. Pang, Transition metal oxides with one-dimensional/one-dimensional-analogue nanostructures for advanced supercapacitors, J. Mater. Chem. A. 5 (2017) 8155–8186. https://doi.org/10.1039/C7TA02454A.

[7] T. Noor, M. Ammad, N. Zaman, N. Iqbal, L. Yaqoob, H. Nasir, A Highly Efficient and Stable Copper BTC Metal Organic Framework Derived Electrocatalyst for Oxidation of Methanol in DMFC Application, Catal. Letters. 149 (2019) 3312–3327. https://doi.org/10.1007/s10562-019-02904-6.

[8] A. Borenstein, O. Hanna, R. Attias, S. Luski, T. Brousse, D. Aurbach, Carbon-

based composite materials for supercapacitor electrodes: A review, J. Mater. Chem. A. 5 (2017) 12653–12672. https://doi.org/10.1039/c7ta00863e.

[9] M. Noked, S. Okashy, T. Zimrin, D. Aurbach, Composite carbon nanotube/carbon electrodes for electrical double-layer super capacitors, Angew. Chemie - Int. Ed. 51 (2012) 1568–1571. https://doi.org/10.1002/anie.201104334.

[10] I. Mazurenko, M. Etienne, G. Francius, I. Vakulko, A. Walcarius, Macroporous carbon nanotube-carbon composite electrodes, Carbon N. Y. 109 (2016) 106–116. https://doi.org/10.1016/j.carbon.2016.07.050.

[11] Y. Qiu, G. Li, Y. Hou, Z. Pan, H. Li, W. Li, M. Liu, F. Ye, X. Yang, Y. Zhang, Vertically aligned carbon nanotubes on carbon nanofibers: A hierarchical three-dimensional carbon nanostructure for high-energy flexible supercapacitors, Chem. Mater. 27 (2015) 1194–1200. https://doi.org/10.1021/cm503784x.

[12] Y. Dong, H. Pang, H. Bin Yang, C. Guo, J. Shao, Y. Chi, C.M. Li, T. Yu, Carbon-based dots co-doped with nitrogen and sulfur for high quantum yield and excitation-independent emission, Angew. Chemie - Int. Ed. 52 (2013) 7800–7804. https://doi.org/10.1002/anie.201301114.

[13] J. Chen, C. Li, G. Shi, Graphene materials for electrochemical capacitors, J. Phys. Chem. Lett. 4 (2013) 1244–1253. https://doi.org/10.1021/jz400160k.

[14] J. Yang, Y. Zhai, Y. Deng, D. Gu, Q. Li, Q. Wu, Y. Huang, B. Tu, D. Zhao, Direct triblock-copolymer-templating synthesis of ordered nitrogen-containing mesoporous polymers, J. Colloid Interface Sci. 342 (2010) 579–585. https://doi.org/10.1016/j.jcis.2009.10.037.

[15] G.P. Hao, W.C. Li, D. Qian, G.H. Wang, W.P. Zhang, T. Zhang, A.Q. Wang, F. Schüth, H.J. Bongard, A.H. Lu, Structurally designed synthesis of mechanically stable poly(benzoxazine-co- resol)-based porous carbon monoliths and their application as high-performance CO2 capture sorbents, J. Am. Chem. Soc. 133 (2011) 11378–11388. https://doi.org/10.1021/ja203857g.

[16] X. Wang, C.G. Liu, D. Neff, P.F. Fulvio, R.T. Mayes, A. Zhamu, Q. Fang, G. Chen, H.M. Meyer, B.Z. Jang, S. Dai, Nitrogen-enriched ordered mesoporous carbons through direct pyrolysis in ammonia with enhanced capacitive performance, J. Mater. Chem. A. 1 (2013) 7920–7926. https://doi.org/10.1039/c3ta11342f.

[17] N.P. Wickramaratne, J. Xu, M. Wang, L. Zhu, L. Dai, M. Jaroniec, Nitrogen enriched porous carbon spheres: Attractive materials for supercapacitor electrodes and CO2 adsorption, Chem. Mater. 26 (2014) 2820–2828. https://doi.org/10.1021/cm5001895.

[18] D. Wu, Z. Li, M. Zhong, T. Kowalewski, K. Matyjaszewski, Templated synthesis of nitrogen-enriched nanoporous carbon materials from porogenic organic precursors prepared by ATRP, Angew. Chemie - Int. Ed. 53 (2014) 3957–3960. https://doi.org/10.1002/anie.201309836.

[19] V. Chabot, D. Higgins, A. Yu, X. Xiao, Z. Chen, J. Zhang, A review of graphene and graphene oxide sponge: Material synthesis and applications to energy and the environment, Energy Environ. Sci. 7 (2014) 1564–1596. https://doi.org/10.1039/c3ee43385d.

[20] G. Wang, L. Zhang, J. Zhang, A review of electrode materials for electrochemical supercapacitors, Chem. Soc. Rev. 41 (2012) 797–828. https://doi.org/10.1039/C1CS15060J.

[21] X. Zhuang, F. Zhang, D. Wu, X. Feng, Graphene coupled schiff-base porous polymers: Towards nitrogen-enriched porous carbon nanosheets with ultrahigh electrochemical capacity, Adv. Mater. 26 (2014) 3081–3086. https://doi.org/10.1002/adma.201305040.

[22] G.A. Ferrero, A.B. Fuertes, M. Sevilla, N-doped porous carbon capsules with tunable porosity for high-performance supercapacitors, J. Mater. Chem. A. 3 (2015) 2914–2923. https://doi.org/10.1039/c4ta06022a.

[23] J. Yan, Z. Fan, T. Wei, J. Cheng, B. Shao, K. Wang, L. Song, M. Zhang, Carbon nanotube/MnO2 composites synthesized by microwave-assisted method for supercapacitors with high power and energy densities, J. Power Sources. 194 (2009) 1202–1207. https://doi.org/10.1016/j.jpowsour.2009.06.006.

[24] Y. Qian, S. Lu, F. Gao, Preparation of MnO2/graphene composite as electrode material for supercapacitors, J. Mater. Sci. 46 (2011) 3517–3522. https://doi.org/10.1007/s10853-011-5260-y.

[25] J. Yan, Z. Fan, T. Wei, W. Qian, M. Zhang, F. Wei, Fast and reversible surface redox reaction of graphene-MnO2 composites as supercapacitor electrodes, Carbon

N. Y. 48 (2010) 3825–3833. https://doi.org/10.1016/j.carbon.2010.06.047.

[26] P. Simon, Y. Gogotsi, Materials for electrochemical capacitors, Nat. Mater. 7 (2008) 845–854. https://doi.org/10.1038/nmat2297.

[27] M. Ritala, Atomic layer deposition, in: High-K Gate Dielectr., Academic Press, 2003: pp. 17–64. https://doi.org/10.1365/s35144-011-0169-4.

[28] A.E. Fischer, K.A. Pettigrew, D.R. Rolison, R.M. Stroud, J.W. Long, Incorporation of homogeneous, nanoscale MnO2 within ultraporous carbon structures via self-limiting electroless deposition: Implications for electrochemical capacitors, Nano Lett. 7 (2007) 281–286. https://doi.org/10.1021/nl062263i.

[29] R. Warren, F. Sammoura, F. Tounsi, M. Sanghadasa, L. Lin, Highly active ruthenium oxide coating via ALD and electrochemical activation in supercapacitor applications, J. Mater. Chem. A. 3 (2015) 15568–15575. https://doi.org/10.1039/c5ta03742e.

[30] Z.S. Wu, D.W. Wang, W. Ren, J. Zhao, G. Zhou, F. Li, H.M. Cheng, Anchoring hydrous RuO2 on graphene sheets for high-performance electrochemical capacitors, Adv. Funct. Mater. 20 (2010) 3595–3602. https://doi.org/10.1002/adfm.201001054.

[31] Q. Wang, L. Jiao, H. Du, Y. Wang, H. Yuan, Fe3O4 nanoparticles grown on graphene as advanced electrode materials for supercapacitors, J. Power Sources. 245 (2014) 101–106. https://doi.org/10.1016/j.jpowsour.2013.06.035.

[32] P.C. Gao, P.A. Russo, D.E. Conte, S. Baek, F. Moser, N. Pinna, T. Brousse, F. Favier, Morphology Effects on the Supercapacitive Electrochemical Performances of Iron Oxide/Reduced Graphene Oxide Nanocomposites, ChemElectroChem. 1 (2014) 747–754. https://doi.org/10.1002/celc.201300087.

[33] M. Li, G. Sun, P. Yin, C. Ruan, K. Ai, Controlling the formation of rodlike V2O5 nanocrystals on reduced graphene oxide for high-performance supercapacitors, ACS Appl. Mater. Interfaces. 5 (2013) 11462–11470. https://doi.org/10.1021/am403739g.

[34] T. Nathan, A. Aziz, A.F. Noor, S.R.S. Prabaharan, Nanostructured NiO for electrochemical capacitors: Synthesis and electrochemical properties, in: J. Solid State Electrochem., Springer, 2008: pp. 1003–1009.

https://doi.org/10.1007/s10008-007-0465-3.

[35] N.B. Trung, T. Van Tam, D.K. Dang, K.F. Babu, E.J. Kim, J. Kim, W.M. Choi, Facile synthesis of three-dimensional graphene/nickel oxide nanoparticles composites for high performance supercapacitor electrodes, Chem. Eng. J. 264 (2015) 603–609. https://doi.org/10.1016/j.cej.2014.11.140.

[36] R. Rajendran, L.K. Shrestha, R.M. Kumar, R. Jayavel, J.P. Hill, K. Ariga, Composite Nanoarchitectonics for Ternary Systems of Reduced Graphene Oxide/Carbon Nanotubes/Nickel Oxide with Enhanced Electrochemical Capacitor Performance, J. Inorg. Organomet. Polym. Mater. 25 (2015) 267–274. https://doi.org/10.1007/s10904-014-0102-4.

[37] O. Fleker, A. Borenstein, R. Lavi, L. Benisvy, S. Ruthstein, D. Aurbach, Preparation and Properties of Metal Organic Framework/Activated Carbon Composite Materials, Langmuir. 32 (2016) 4935–4944. https://doi.org/10.1021/acs.langmuir.6b00528.

[38] K.M. Choi, H.M. Jeong, J.H. Park, Y.-B. Zhang, J.K. Kang, O.M. Yaghi, Supercapacitors of Nanocrystalline Metal–Organic Frameworks, ACS Nano. 8 (2014) 7451–7457. https://doi.org/10.1021/nn5027092.

Chapter 3: Review on Experimentation and Characterization Methods

3.1 Synthesis Method

For the proper synthesis of the catalyst material in the lab, many methods have been devised. Among them, some methods require special equipment while others can be performed without them. Choice of the catalyst synthesis process to form required NPs mainly rests on the preferred size, suitable properties of the surface, and the kind of material that is concerned such as semiconductors, metals, polymers, ceramics, etc. These methods have been researched and improved to increase the yield of our catalyst, obtain better structural properties and purity. Some of these methods have been discussed below:

3.1.1 Solvothermal Synthesis

It is a technique used for making a range of materials like semiconductors, metals, polymers, and ceramics. The method involves a solvent at moderate to high pressure (typically between 1atm and 10,000 atm) and temperature (from 100 °C to 1000°C) which helps precursors in interaction during synthesis. If the solvent used is water, then the process is known as the "hydrothermal process." The conditions of the hydrothermal synthesis process are usually kept at the supercritical temperature of water (374 °C). This method can be performed to make a wide variety of geometries such as thin films, single crystals, bulk powders, and nanocrystals. In addition, the formation (rod (2D), sphere (3D), and wire (1D) of crystals are organized by the control of chemical of interest concentration, solvent supersaturation, and control on kinetic. It can be used to form stagnant and thermodynamically stable forms involving novel elements that are not easily constructed from other synthetic paths. This review will emphasize some recent advances including the solvothermal process and nanocrystalline because in the last decade 80% of the literature focused on nanocrystals [1].

3.1.1.1 Synthesis of ZIF-8

ZIF-8 is usually prepared using solvothermal method. Simple scheme is used to synthesize ZIF-8. Metal salt zinc nitrate hexahydrate is mixed with methanol to form a solution.

Organic linker 2-methyleimidazole is separately mixed with methanol to form another solution. Ratio of metal salt and organic linker is varied according to the morphology requirement and application. After that both solutions are mixed at room temperature while stirring. After 30 minutes of stirring solution is placed for 24 hours aging. After aging is finished purple precipitate settles down. Precipitate is thoroughly washed with ethanol and deionized water. Collected precipitate is dried in vacuum oven at 60 °C for 12 hours. After vacuum drying, sample is grinded to collect fine powder.

3.1.2 Hydrothermal Synthesis

This method is used to synthesize materials that require special conditions for the synthesis. Also, this method helps control the structure, morphology, and other properties of the material. Metal oxides, halides, composites that require specific temperature as well as pressure are usually synthesized by this method. The nanoparticles obtained by this method have characteristic properties. This method normally requires the use of an autoclave device in which temperature and pressure can be simultaneously controlled. The main significance of this process is the ability to synthesize a wide number of NPs that have upgraded composition, size, structure, and chemistry of surface that is reasonably cheap.

3.1.3 Pyrolysis

During pyrolysis, organic matter is decomposed into no condensable gases, condensable liquids, and biochar or charcoal as a residual solid product in an inert environment without oxygen.

3.1.4 Carbonization

Carbonization is a thermal decomposition process that produces a carbonaceous residue (while simultaneously removing the distillate) from organic substances. Pyrolysis is the oldest direct method of producing liquids from coal. It involves heating coal and capturing volatilized liquids, leaving behind a hydrogen-depleted carbon residue. In addition to the small amount of liquid that is produced (less than 20 percent), the mixture of chemicals and water contamination makes for a poor product. While organic matter is decomposed at high temperatures and the distillate is removed at the same time, carbonization is

primarily used to produce a carbonaceous residue known as coke. Carbonization of ZIF is performed to covert ZIF in to nano porous carbon and carbon nano tubes.

3.2 Characterization Techniques

3.2.1 X-Ray Diffraction (XRD)

This is one of the most important and common material characterization technique which provides information about the morphology, components, and crystallite size of the material. It uses X-ray radiations that pass through the material at an angle to the source. The diffraction angle is calculated, and the intensity is recorded. At an angle how many radiations deflect from a specific plane on the material gives information regarding its structure morphology.

To find evidence about the configuration of X-ray diffraction (XRD) of crystalline materials depend on the double particle/wave nature of X-rays. Identification and characterization of materials centered on their X-ray form are the major uses of the procedure. When a monochromatic X-rays incident beam contacts an object material the first outcome that takes place is atoms within the target substance scatter those X-rays as shown in Figure 3.1. The spread X-rays undertake destructive and constructive interference in the substances having proper structure (i.e. crystalline), which is called diffraction. The X-rays diffraction by crystals is described by Bragg‟s Law,

$$n(\lambda) = 2d\ Sin(\theta) \qquad (6)$$

The shape and size of the materials unit cell determine directions of likely diffractions. The atom's arrangement in the crystal structure affects the diffracted wave intensities. Many materials are not one crystal rather are comprised of little, small crystallites in all likely directions which are called polycrystalline powder or aggregate. When a material with casually focused crystallites is put in an X-ray, the beam will view all available interatomic planes. If the experimental angle is scientifically altered, then all the available diffraction peaks from the substance will be identified [2].

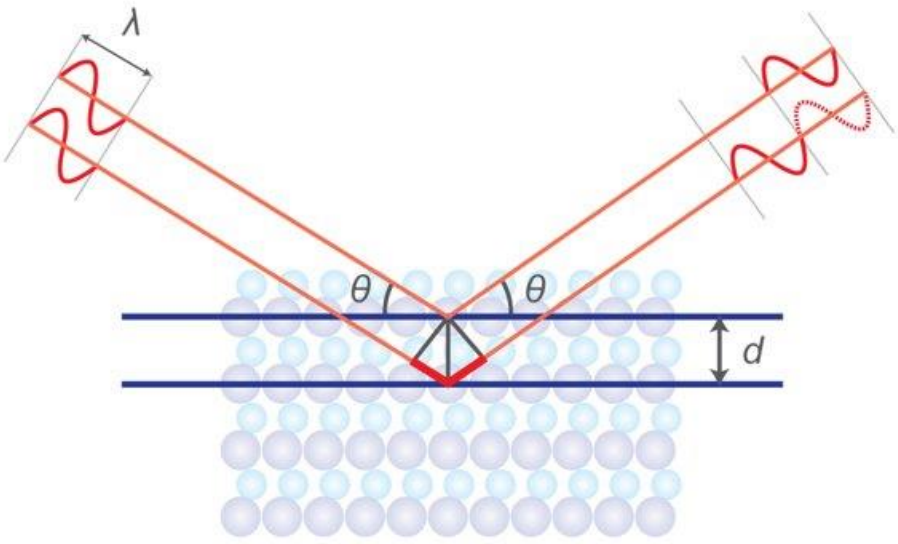

Figure 3-1. The Bragg's Law [1]

3.2.2 Scanning Electron Microscopy

The scanning electron microscope (SEM) utilizes a high-energy electrons-focused ray to produce a wide range of signals at the solid surface of the specimen. The high-energy electrons penetrate through the material and escape through the other end as shown in Figure 3.2. The information of the substance like chemical composition, crystalline structure, external morphology (texture), and materials orientation will be revealed signals of the electron beam and sample interactions. In various applications, a 2-dimensional image is created that shows spatial variations in these properties, and numbers are collected over a particular choice area of the sample surface. The scanning method by simple SEM practices (magnification varying from 20X to around 30,000X, 3-D resolution of 50 to 100 nm) can be used to distinguish the areas that vary in size from about 1 cm to 5 microns in breadth. This method is exclusively valuable in semi quantitatively or qualitatively identifying chemical contents (by EDS), crystal orientations (using EBSD), and crystalline structure. The SEM is proficient in executing analyses of a specific area or point locations on the sample object. Its design and function are quite comparable to the EPMA and significant connections in abilities remain between the two devices [3].

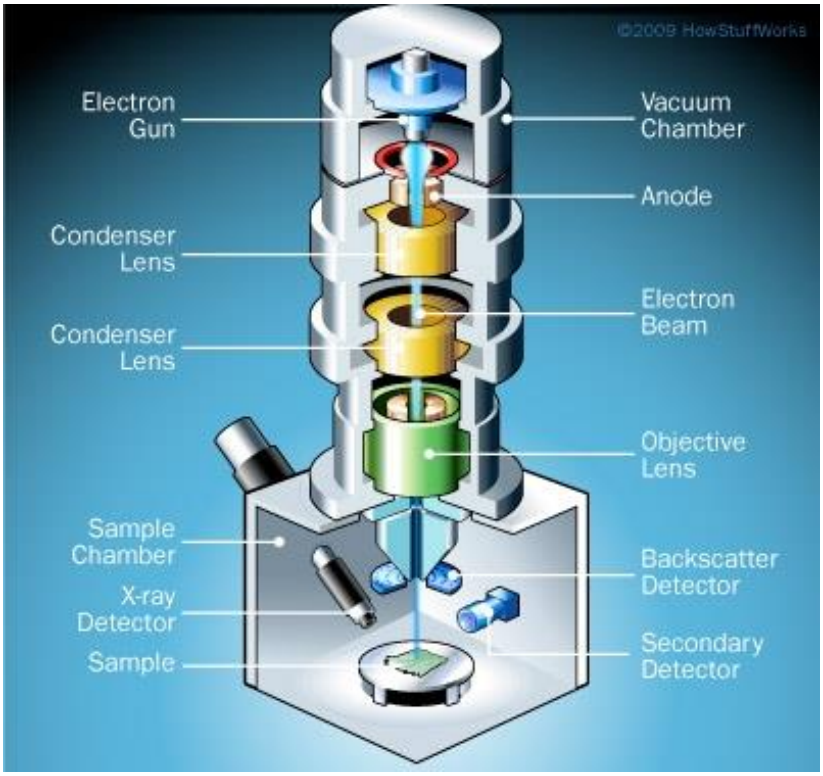

Figure 3-2. Illustration of how SEM works [2].

3.2.3 Energy Dispersive X-ray Spectroscopy (EDX)

EDS is an elemental analysis method used to quantify the number of individual elements present in a nanoparticle. This technique gives the number of substances at a particular point but does not give the overall quantity of each element. It is usually combined with SEM or TEM to get a nanoscale image of particles through them, and EDS performs the analysis of that nanostructure. In the early 1970s, EDS developed into one commercial product and rapidly crossed WDS in popularity. The overall structure of the EDS is very simple because of no moving parts like the rotation detector in WDS. The sensor gathers the X-rays energies signal from all series elements in a sample at a similar time as compared to gathering signals from X-ray wavelength one by one which makes the EDS systems relatively fast as seen in Figure 3.3. The characteristic energy dispersion resolution is around 150–200 eV, which is lower than WDS resolve. The lightest component that can be identified is not C (Z=6) rather O (Z=8). But major benefits like low cost and fast analysis make these disadvantages insignificant [2].

EDS band is a graph between the power of X-rays and the corresponding energies. Both light and heavy elements can be seen in a range of spectrum from 0.1 to 10-20 keV because both M or L lines of heavy elements and K lines of light elements are evident in this array.

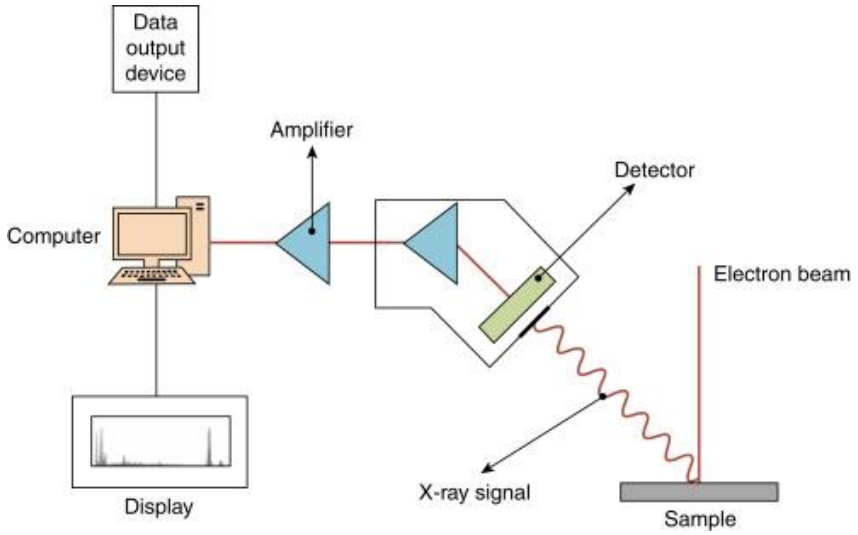

Figure 3-3. Illustration of EDX [3].

3.2.4 Thermo-Gravimetric Analysis

Thermogravimetric analysis (TGA) determines weight losses in a material with a change in temperature in a controlled atmosphere. The major applications of this characterization technique are the measurement of thermal stability, volatile content, moisture, organic linker in a sample, and the percent composition of components in a compound. The principle is that the temperature is gradually increased from zero to the required final temperature in a specific gas atmosphere which maybe Ar, air or some other gas. Now when temperature increases the contents in the sample start to evaporate. Moisture is usually the first content that removes from the sample so a change in mass of sample occurs. This mass is measured on the weight balance continuously during the process which is placed outside the furnace Figure 3.4. After moisture other volatile contents like organic residues start to escape. The stability of the sample can be defined as the temperature at which the material starts to decompose which is the main point in the curve. After that the line drops sharply causing a major loss in material. This point is called the decomposition temperature and determines the stability of material. The weight of the material is mapped against temperature or time to demonstrate the thermal changes in the

sample, for instance, the loss of solvent, loss of water of hydration, and the decomposition of the material. At the end of the process, the final mass residue is noted, and the total mass loss is calculated [4].

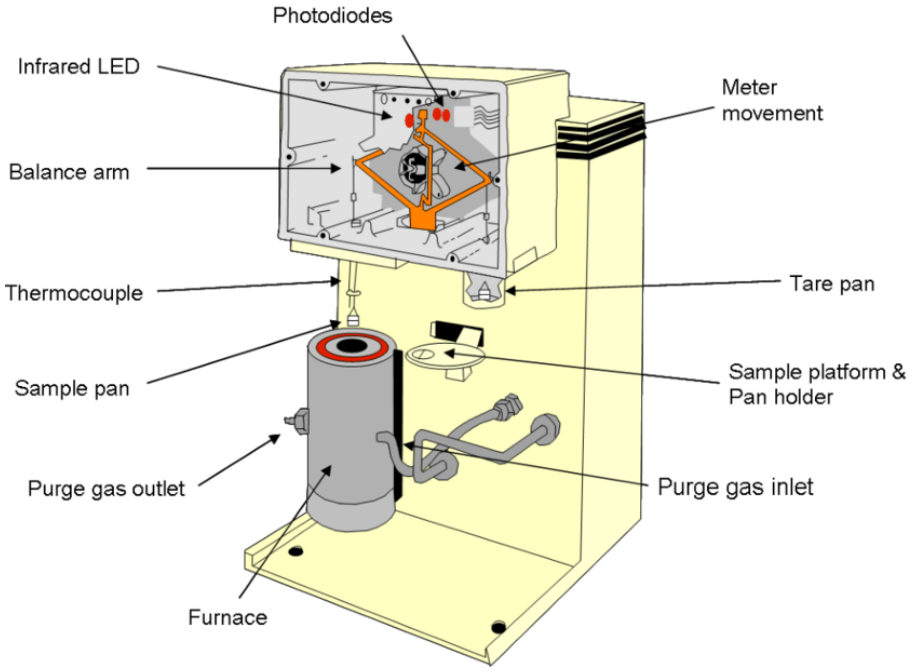

Figure 3-4. Schematic of TGA [4].

3.2.5 Fourier Transform Infrared Spectroscopy

Fourier transform infrared spectroscopy is the preferred technique for infrared spectroscopy. When IR radiation passes through a material, some of the incident radiation gets absorbed in the material while the rest is transmitted Figure 3.5. The detector at the other end detects the transmitted radiation and sets out a signal that is basically represented in the form of a spectrum and it demonstrates the molecular nature of the material [5].

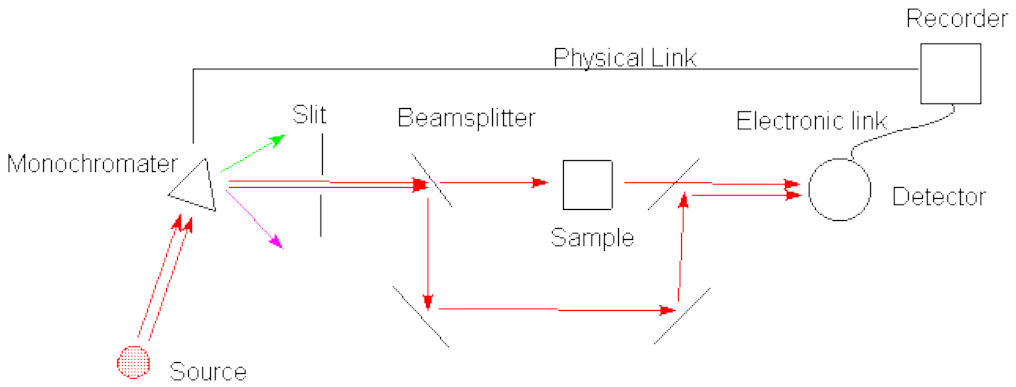

Figure 3-5. Schematic diagram of FTIR [6].

3.3 Electrochemical Testing

3.3.1 Slurry/Ink Formation

There are many substrates available for using as working electrode for example Glassy carbon electrode, nickel foam and carbon cloth. For every substrate method of ink formation is different. For glassy carbon we use ethanol as solvent and nafion (5 wt.% ion solution in lower aliphatic alcohols) as binder. Purpose of binder is to bind the active electrode material so that it sticks to the electrode. For nickel foam and carbon cloth we use PVDF as binder and n-methylepropyrilidine (NMP) as solvent. Carbon black/graphite powder/super-p is also added to the slurry. PVDF binder causes resistance that ultimately mitigate the overall conductivity of the active material. Purpose of carbon black is to cope with the reduced activity of active material caused by the PVDF binder. After mixing the required recipe, solution is sonicated for 4 hours to make homogenous suspension.

3.4 Electrochemical Techniques

When glassy carbon electrode is fabricated, it is dried at 60 degrees Celsius for 30 minutes. After that electrochemical testing is performed. For super capacitors three techniques are performed in electrochemical workstation.

- Cyclic Voltammetry (CV)
- Chronopotentiometry
- Electrochemical Impedance Spectroscopy (EIS)

3.4.1 Cyclic Voltammetry

Cyclic voltammetry (CV) is a great and common technique of electrochemistry usually used to study the oxidation and reduction procedures of molecular species. It is helpful to investigate chemical reactions initiated by electron transfer, which comprises catalysis. This electrochemical technique involves the running of the workstation through a complete cycle. The potential range was input into the software which is applied across the two electrodes. Scan rate, sample interval, sensitivity was given for each run along with several segments. Two segments make one complete cycle. The cyclic voltammetry gives information of the current changing with voltage as shown in Figure 3.6 [10]. When CV is performed the current passes through an external circuit and electrons start to flow from anode to cathode. For CV, beaker cell was used in three electrode system. Working electrode was glassy carbon, counter electrode was platinum wire and reference electrode was Ag/AgCl [6].

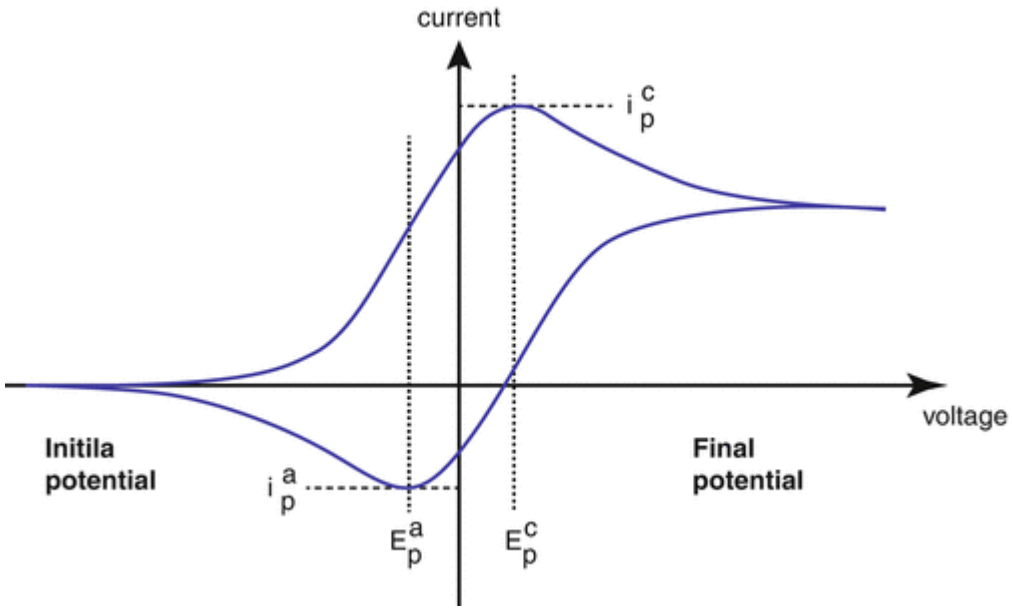

Figure 3-6. CV profile [7].

3.4.2 Chronopotentiometry

Chronopotentiometry is an electrochemical analysis method where the electrodes are subjected to a constant flow of current in order to the cause a constant reduction of the electroactive material Figure 3.7. This method is differentiated from constant-current coulometric analysis and coulometric titrimetry1 because in this technique the applied

current appears to be significantly large so that the efficiency of current required for the reduction of the material is reduced below 100% within a few seconds.

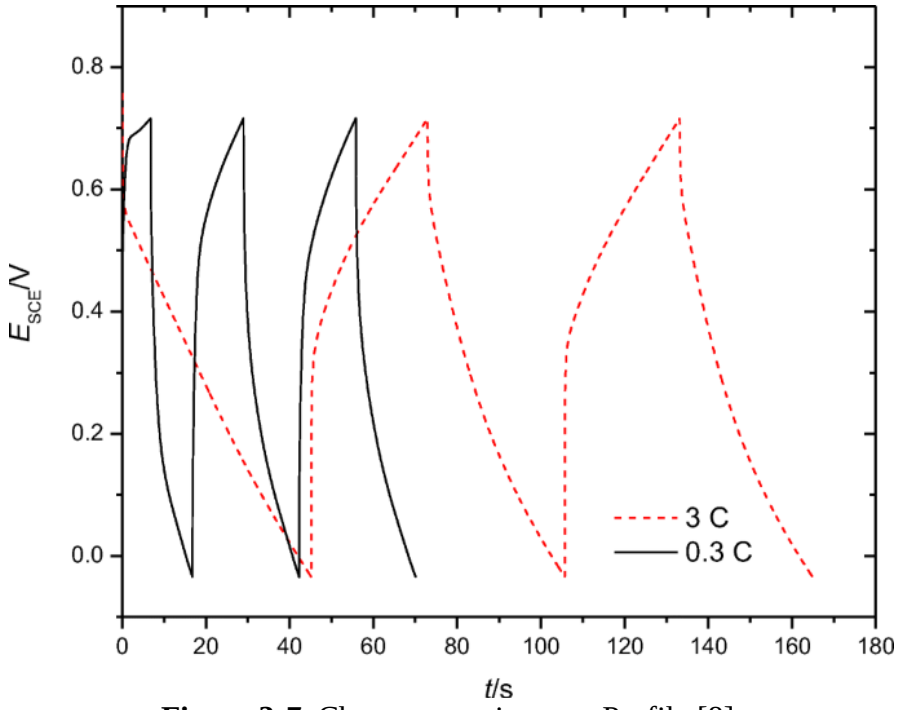

Figure 3-7. Chronopotentiometry Profile [8].

3.4.3 Electrochemical Impedance Spectroscopy (EIS)

This technique of electrochemical workstation allows us to measure the resistivity of our system. This includes resistance of electrolyte, ohmic loss and or activation losses. Electrical resistance is the measure of the of a circuit element that resists current flow.

$$R = E/I \quad (7)$$

According to Ohm's law, R is the resistance which is defined as the ratio of voltage (E), and current (I). This known law use is limited to only one circuit element, the ideal resistor. An ideal resistor has several simplifying properties:

- Ohm's Law is followed at every range of current and voltage.
- Resistance is not dependent on the frequency.
- The voltage passing through a resistor and the AC current are in a single phase.

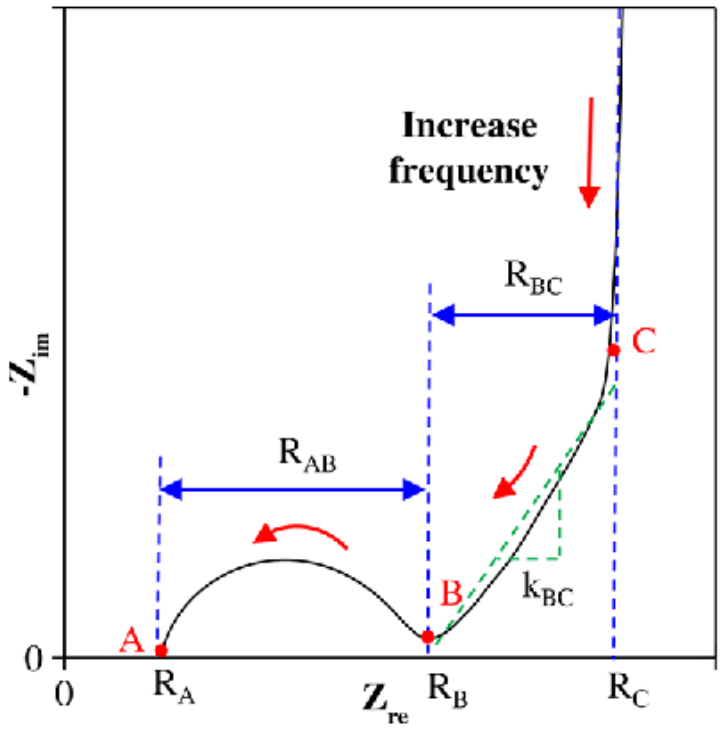

Figure 3-8. EIS Profile (Nyquist Plot) [9].

3.5 Electrochemical Parameters

The determination of the energy density and power density is very important to evaluate the efficiency of a supercapacitor for real-life applications. Cyclic voltammetry (CV) and chronopotentiometry are the techniques that can confirm the energy and power densities by using the following equations:

The specific capacitance (C, Fg^{-1}) can be determined using cyclic voltammetry:

$$C_s = \frac{\int IdV}{2mv\Delta V} \tag{8}$$

Here, ∫IdV is the integral area of the CV curves, m represents the mass, n represents the scan rate used to perform the analysis, and the voltage window of the process is represented by V.

$$E = \frac{1}{2}\frac{C_m \Delta V^2}{3.6} \tag{9}$$

Here, E is the symbol for energy density. The specific power (W/kg) defines how rapidly a device is able to deliver energy under a constant current density to external loads. The maximum specific power is calculated as:

$$P = \frac{E}{\Delta t} \times 3600 \tag{10}$$

Here, P represents the maximum power that can be achieved by a supercapacitor.

Summary

This chapter initially discusses different chemical synthesis methods like solvothermal and hydrothermal method. After that material characterization techniques have been studied i.e., XRD, SEM, EDS, TGA, BET and XPS . Main principle of these techniques has been noted down along with diagrams. After that the whole electrochemical testing process implemented was explained including ink formation, ink deposition on substrate and electrochemical performance determination using various techniques like CV, CP, and EIS with a three-electrode system.

List of References

[1] T. Takahashi, K. Kuwabara, and M. Shibata, "Solid-state ionics - conductivities of Na+ ion conductors based on NASICON," *Solid State Ionics*, vol. 1, no. 3–4, pp. 163–175, 1980, doi: 10.1016/0167-2738(80)90001-6.

[2] N. S. Mohamed, R. H. Y. Subban, and R. Rusdi, "Enhancement of electrical properties of NASICON-type solid electrolytes (LiSn2P3O12) via aluminium substitution," *J. Sci. Adv. Mater. Devices*, vol. 5, no. 3, pp. 368–377, 2020, doi: 10.1016/j.jsamd.2020.06.003.

[3] F. Zheng, M. Kotobuki, S. Song, M. O. Lai, and L. Lu, "Review on solid electrolytes for all-solid-state lithium-ion batteries," *J. Power Sources*, vol. 389, no. April, pp. 198–213, 2018, doi: 10.1016/j.jpowsour.2018.04.022.

[4] C.J.Brinker;G.W.Scherer,"Sol-Gel_Science_The_physics_and_chemistry_of_sol-gel_processing_-_Brinker_1990.pdf." p. 462, 1990. doi: 10.1016/S0254-0584(02)00315-2.

[5] S. D. Lee *et al.*, "Composite Electrolyte for All-Solid-State Lithium Batteries: Low-Temperature Fabrication and Conductivity Enhancement," *ChemSusChem*, vol. 10, no. 10, pp. 2175–2181, 2017, doi: 10.1002/cssc.201700104.

[6] J. Lai, W. Niu, R. Luque, and G. Xu, "Solvothermal synthesis of metal nanocrystals and their applications," *Nano Today*, vol. 10, no. 2, pp. 240–267, 2015, doi: 10.1016/j.nantod.2015.03.001.

[7] X. Dong, M. Qi, Y. Tong, and F. Ye, "Solvothermal synthesis of single-crystalline hexagonal cobalt nanofibers with high coercivity," *Mater. Lett.*, vol. 128, pp. 39–41, 2014, doi: 10.1016/j.matlet.2014.04.133.

[8] S. Sōmiya and R. Roy, "Hydrothermal synthesis of fine oxide powders," *Bull. Mater. Sci.*, vol. 23, no. 6, pp. 453–460, 2000, doi: 10.1007/BF02903883.

[9] S. Feng and R. Xu, "New materials in hydrothermal synthesis," *Acc. Chem. Res.*, vol. 34, no. 3, pp. 239–247, 2001, doi: 10.1021/ar0000105.

Chapter 4: Methodology and Experimentation

4.1 Chemical Reagents

All the chemicals were purchased from Sigma Aldrich and used in their original state. Zinc nitrate hexahydrate ($Zn(NO_3)_2.6H_2O$, 99%), ferrous sulfate heptahydrate ($FeSO_4.7H_2O$, 99%), cobalt nitrate hexahydrate ($Co\ (NO_3)_2.6H_2O$, 99%), and 2-methylimidazole (2-MeIM), methanol (CH_3OH) was used during synthesis.

4.2 Material Synthesis

4.2.1 Synthesis of Fe-Co/ZIF8

Fe-Co/ZIF8 was synthesized using a simple co-precipitation technique as illustrated in scheme 1. $Zn\ (NO_3)_2.6H_2O$, $FeSO_4.7H_2O$ and $Co\ (NO_3)_2.6H_2O$ with a molar ratio of 1:2:1 was dissolved in 150 ml methanol to make solution A. 2-MeIM was dissolved in 150 ml methanol to make solution B, which was then gently mixed into solution A with the linker to metal precursor ratio of (8:1). After 4 hours of stirring, the solution was aged for 24 hours. The precipitates were centrifuged for 5 minutes at 4000 rpm, then it was thoroughly washed with methanol and DI multiple times and set to dry in a drying oven at 70 °C. Fe-Co/ZIF8 precipitate powder was obtained after drying.

4.2.2 Carbonization of Fe-Co/NPC-900

The Fe-Co/ZIF8 (1 mg) product was heated at 900 ℃ in a nitrogen N_2 environment for 2 h in the tube furnace. From the ambient temperature to the furnace's target temperature, the temperature was raised exponentially with a ramp of 5 ℃/min. The powder was then annealed for 5 h and cooled to room temperature naturally. The black Fe-Co/NPC-900 powder was obtained. The mass ratio (2:1) was optimized process for ZIF/NPC-900, Fe/NPC-900, Co/NPC-900, and ZIF/NPC-900, respectively.

4.3 Material Characterization

The phase assembly and sample purity were examined using a Bruker D8 Advance diffractometer with LYNXEYE detector and Cu-Kα radiation. X-ray diffraction (XRD) was taken in a range of 2θ (10° - 80°) with a step size of 0.02°. Scanning electron

microscopy (SEM, Tescan Vega 3) was used to validate the material morphology. X-ray photoelectron spectroscopy (XPS) was measured using VG Multilab 2000 equipment with Al as the target anode for the X-ray source PHI 5000 Versa Probe (Ulvac -PHI, Japan). Thermogravimetric analysis (TGA) was done in N2 environment using the Discovery TGA 5500. The surface areas and pore size distribution of synthesized electrode material were measured using a Nova Win 20e (Quantachrome, Virginia, USA) equipment, and the degassing was done at 120 ℃ samples were degassed at 120 ℃ under vacuum.

4.4 Electrochemical Measurements

CH Instruments electrochemical workstation model 660E was used to investigate the electrochemical behavior of all the synthesized electrodes including cyclic voltammetry (CV), galvanostatic charge-discharge (GCD), and electrochemical impedance spectroscopy (EIS) in a three-electrode configuration. Ag/AgCl and platinum wire was used as reference and counter electrode respectively. The electrochemical measurements were conducted out in a 6 M KOH electrolyte using glassy carbon (GC) as a working electrode. 80 µl ethanol, 20 µl Nafion binder (5% ion solution), and 2 mg active electrode material were mixed and sonicated for 4 hours to form a homogenous slurry. The slurry was drop cast upon the GC's gleaming surface. GC was ready to serve as a working electrode after 20 minutes of air drying. CV profiles were collected at a sweep rate of 10, 20, 30, 40, 50, and 100 mV s^{-1} within a potential range of -0.4 to 0.2 V. Chronopotentiometry was employed to obtain GCD curves within the potential window of -0.4 to 0.2 V at current densities of 5, 10, 15, 20, 30 A g^{-1}. The frequency range from 0.01 Hz to 100 kHz was used to measure EIS to obtain a Nyquist plot at an amplitude of 0.005 V.

Summary

This chapter includes the total experimentation that was involved in the research process. The synthesis process of Fe-Co/ZIF8, carbonization of Fe-Co/NPC-900 based nitrogen doped carbon and their characterization techniques used were thoroughly demonstrated in the chapter. Finally, the electrochemical testing techniques which were used on electrochemical workstation and the testing parameters are discussed.

List of References

[1] W. Yang, X. Shi, Y. Li, H. Pang, Manganese-doped cobalt zeolitic imidazolate framework with highly enhanced performance for supercapacitor, J. Energy Storage. 26 (2019) 1–7. https://doi.org/10.1016/j.est.2019.101018.

Chapter 5: Results and Discussion

5.1 Material Characterization

5.1.1 X-ray Diffraction (XRD)

XRD patterns of all the samples before and after pyrolysis are depicted in Figure 5.1 to compare with pure ZIF8. All samples displayed a succession of sharp peaks, indicating excellent crystallization order. The XRD peaks of Fe/Co-ZIF8 were like the pure ZIF-8 XRD patterns, showing that the structure of ZIF8 remained unaltered Figure 5.1(a). The XRD pattern of ZIF8/NPC-900 shown in Figure 5.2(b) represented two wide peaks at 2θ = 25°, 44° which corresponds to graphitic carbon planes (002) and (101), respectively. [1, 2]. As the boiling point of zinc is 907 ℃, after carbonization at a high temperature no diffraction peak of metallic zinc appeared as shown in Figure 5.2 (b). Fe/NPC-900 diffraction peaks at 26.5° and 44.7° (JCPDS# 87-0722) were assigned to carbon (002) and (110) planes, respectively. The calculated d spacing of ZIF8/NPC-900, Co/NPC-900, Fe/NPC-900, and Fe-Co/NPC-900 was 0.37 nm, 0.35 nm, 0.32 nm, and 0.36 nm, respectively, which affects the broadness of represented peaks of with metal and without metal doped prepared samples. The broad diffraction peaks of ZIF8/NPC-900 suggest that the phase purity is not affected by the incorporation of zinc ions. Co/NPC-900 exhibited diffraction peaks at 2θ=41.7°, 44.2°, and 51.5° can be indexed to the (100), (111), and (200) crystal planes of metallic cobalt (JCPDS# 15-0806), respectively. Carbon layers covered the metal and blocked protons from diffusing, resulting in residual metal in Co/NPC-900 after annealing at high temperature as confirmed by the XPS Co2p spectrum Figure 5.5(b). Fe-Co/NPC-900 diffraction peaks located at 25.6° and 43° in Figure 5.1(b) correspond to (002) and (100) crystal planes (JCPDS# 49-1568) of graphitic carbon, respectively. The high degree of graphitic carbon was achieved at 900 ℃ with negligible peaks of doped metals. Porous morphology and hollow surface intrude more N atoms into the lattice suggesting that the precursor's crystalline structure transforms into an amorphous phase.

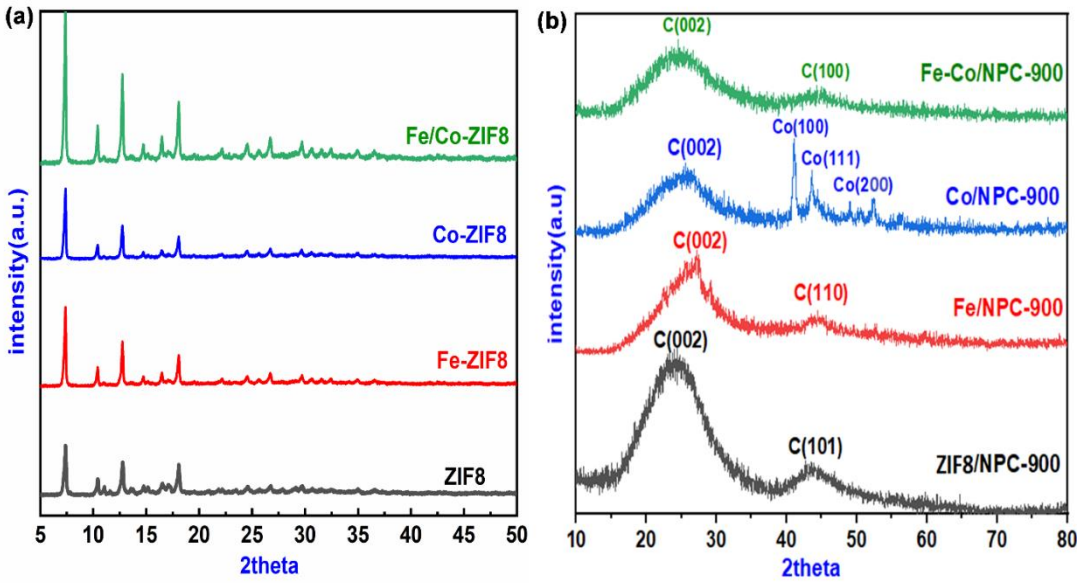

Figure 5-1. XRD pattern of samples (a) before pyrolysis ZIF8 (black), Co-ZIF8(red), Fe-ZIF8(blue) and Fe/Co-ZIF8(green) (b) After pyrolysis ZIF8/NPC-900(black), Fe/NPC-900(red), Co/NPC-900(blue) and Fe-Co/NPC-900(green).

5.1.2 Scanning Electron Microscopy (SEM)

The electron micrograph obtained from pyrolyzed materials depict several agglomerations of particles and shows that this material comprises particles with different particle size without any defined geometrical shapes as shown in Figure 5.2. The morphology of ZIF8/NPC-900 at 900 ℃ with particle size 0.5 nm at 20 µm is sheet-like threads extending from the agglomerates, as illustrated in Figure 5.2(a). On the other hand, the surface roughness of the Fe/NPC-900 with a particle size of 300 nm, becomes more substantial and homogenous as shown in Figure 5.2(c). This was due to the formation of pseudo-mesoporous structures caused by the accumulation of uniform particles. Furthermore, certain Co/NPC-900 (dark subareas) are uniformly distributed throughout the carbon lamellar structures with an average particle size of 5 nm having the same morphology as Fe/NPC-900. It was observed that the particle size of obtained Fe-Co/NPC-900 was reduced by roughly 10 nm due to the shrinking of organic ligands during the pyrolysis in an inert atmosphere and producing a more porous shell-like structure as shown in Figure 5.2(e). As a result, the Fe-Co/NPC-900 had a large surface area measured by BET). As illustrated in Figure 5.2 (b,d,f,h) EDS results confirmed the presence of all elements and the successful formation of NPCs after carbonization at high temperatures.

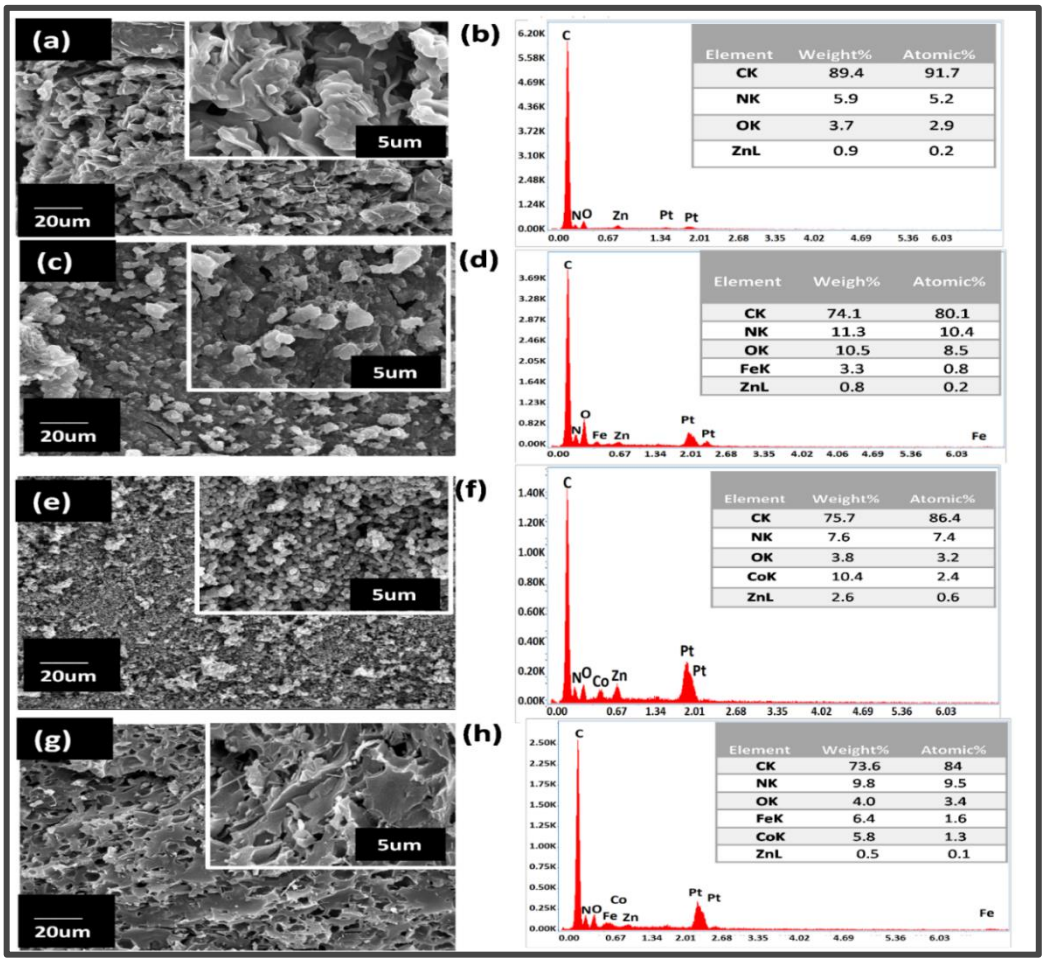

Figure 5-2. SEM images and EDS data of (a,b) ZIF8/NPC-900, (c,d) Fe/NPC-900, (e,f) Co/NPC-900, and (g,h) Fe-Co/NPC-900.

5.1.3 Thermogravimetric Analysis

TGA was used to evaluate the thermal stability of the materials., as shown in Figure 5.3.TGA analysis of the as-prepared samples revealed a breakdown stage at 337 °C to 619 °C under an N2 environment. The initial mass loss was due to the loss of trapped water molecules and weekly coordinated linkers, with subsequent mass loss owing to ligand breakdown up to 619 °C, which was linked to the collapse of the crystal structure [3]. The Fe/NPC-900 (Figure 5.3) exhibited two-step weight reduction. Rapid mass loss begins in all samples at 400 °C, which is typical of carbon-based materials. The elimination of byproducts and certain lower alkyl groups leads to a mass loss in the carbon structure, whereas the reduction of iron oxide into Fe at 570 °C resulted in a mass gain. Co/NPC-

900s and Fe-Co/NPC-900 both exhibited a ~77.49% of weight loss at 350 °C to 600 °C which can be attributed to the decomposition of crystal structure through the second step after gradual decomposition of the residual linker on the surface of materials and encapsulated in the porous framework in presence of hybrid metals (Fe and Co). The product's ultimate weight is 35% of its initial weight. As a result, carbonization at 480 °C results in partially decomposed frameworks, whereas carbonization at temperatures above 570 °C results in entirely disintegrated frameworks into carbon.

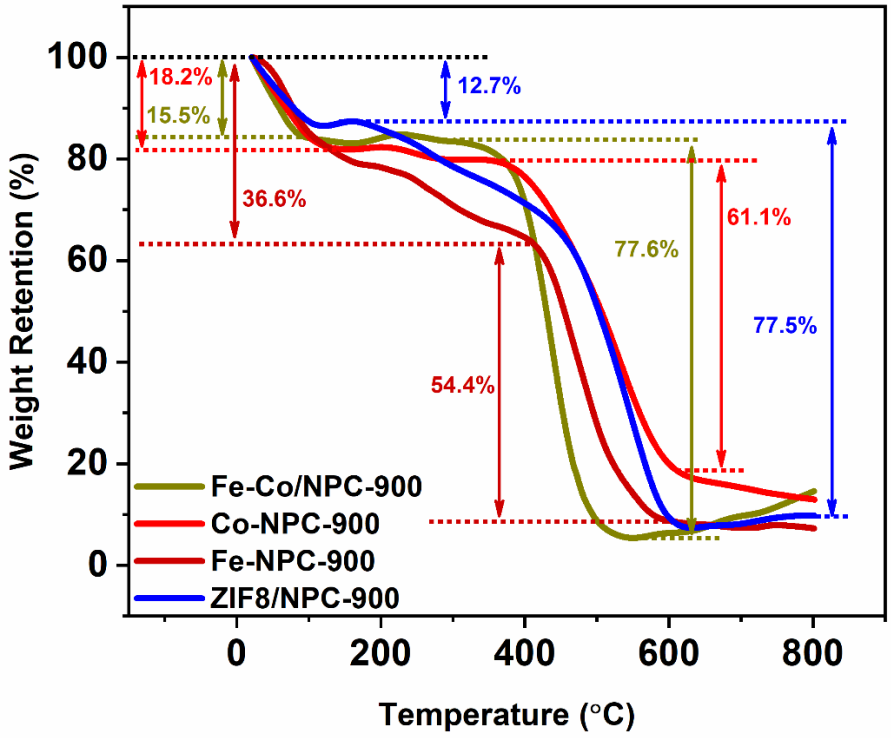

Figure 5-3. TGA profiles of all electrodes.

5.1.4 N_2 Adsorption/Desorption Analysis

Nitrogen adsorption/desorption experiments were performed to examine the surface area and pore size of ZIF8/NPC-900, Co/NPC-900, Fe/NPC-900, and Fe-Co/NPC-900 using the BET method. BET isotherms of all samples are shown in Figure 5.4(a). Fe-Co/NPC-900 had the highest surface area of 933.6 $m^2 g^{-1}$ under high relative pressure (compared to ZIF8/NPC-900 (598.3 $m^2 g^{-1}$), Fe/NPC-900 (513.0 $m^2 g^{-1}$), and Co/NPC-900 (674.6 $m^2 g^{-1}$). The surface areas of ZIF8/NPC-900 decreased significantly due to a degree of bulk shrinkage and the collapse of a well-defined porous structure, formed during the carbonization process. The addition of metals (Fe-Co) and the creation of porous

structures increased the surface area of Fe-Co/NPC-900 and promoted ion transfer at the electrode/electrolyte interface. All four sample curves showed a typical IV isotherm confirmed mesoporous structure, as shown in Figure 5.4(a). As illustrated in Figure 5.4(b), the pore radii were calculated using the desorption component of the BJH pore size distribution. ZIF8/NPC-900, Fe/NPC-900, Co/NPC-900, and Fe-Co/NPC-900 exhibited pore volume of 0.004, 0.09, 0.05 and 0.16 $cm^3\ g^{-1}$, respectively Figure 5.4(b).

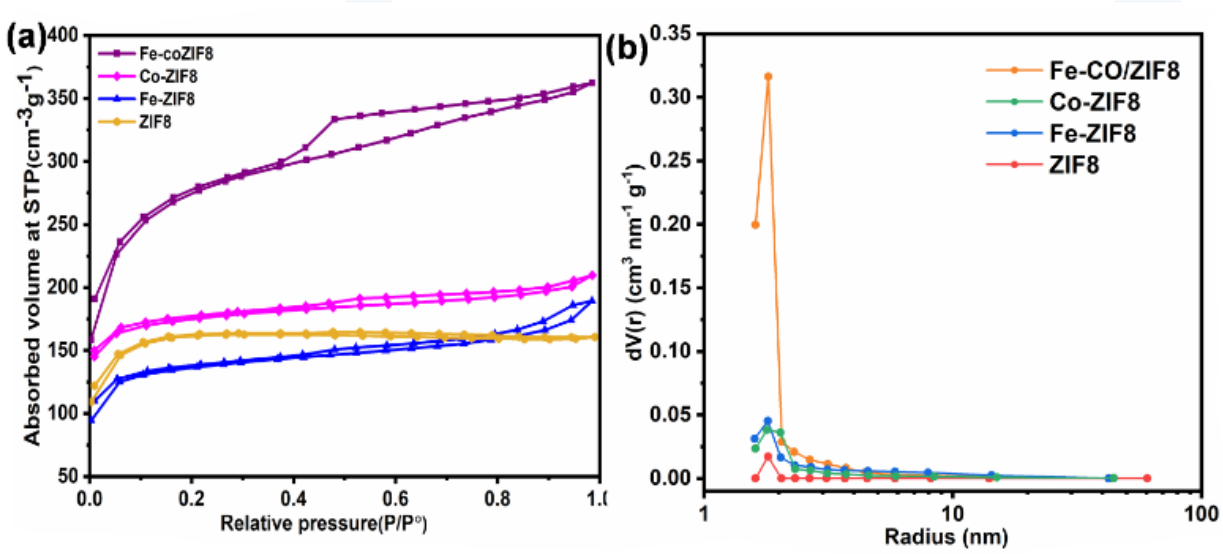

Figure 5-4. (a)Isotherms of electrodes (b)BJH pore size distribution of electrodes.

Table 5-1. Surface area, pore radius, and pore volume of samples as determined by BET.

Electrode material	Surface area ($m^2\ g^{-1}$)	Pore radius (nm)	Pore volume ($cm^3\ g^{-1}$)
ZIF8/NPC-900	598	1.81	0.004
Co/NPC-900	674	1.80	0.05
Fe/NPC-900	513	1.80	0.09
Fe-Co/NPC-900	933	1.79	0.16

5.1.5 X-ray photoelectron spectroscopy

XPS was performed to examine the surface composition and chemical state. For all samples, the content of each element is quantitively measured and given in Table 5.1. The Fe-Co/NPC-900 powder sample clearly demonstrated the presence of Fe, N, C, Co, and O elements Figure 5.5(a) after the one-step pyrolysis at 900 °C. Because of the facile

bonding of Fe-N and Co-N during the pyrolysis process, the nitrogen concentration of Fe-Co/NPC-900 was greater than in the other samples, as shown in Table 2.

The Fe2p spectra may be deconvoluted into two peaks (Fe 2p2/3, Fe 2p1/2) which are related to the 706.0 eV and 719.3 eV, respectively[4]. Following that, the shake-up satellite bands appeared after the development of Fe-Co/NPC-900 suggesting that iron ions are more paramagnetic. In the Co2p XPS spectra, three main peaks of Co, Co-C-N, and Co-C-N at binding energies of 778.4 eV, 779.8 eV, and 781.9 eV, respectively (Figure 5.5(b)[5, 6]. Hence, Fe and Co metallic bonding were produced in Fe-Co/NPC-900, as shown in Figure 5.5(b, c).

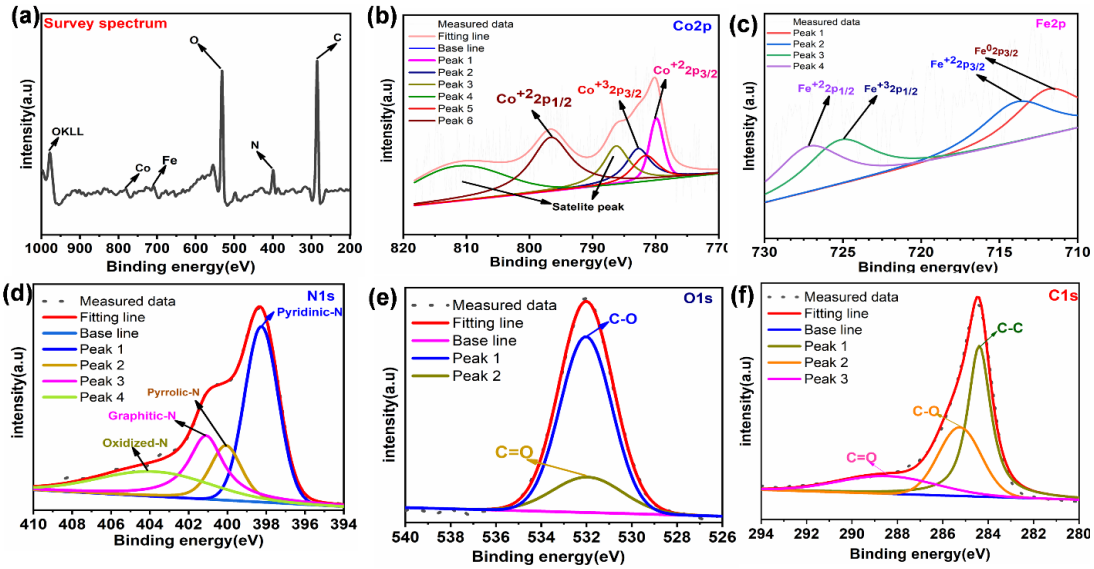

Figure 5-5. (a) XPS survey spectrum of Fe-Co/NPC-900 showing the presence of elements in the sample. Deconvoluted XPS spectra of (b) Co2p, (c) Fe2p, (d) N1s, (e) C1s, and (f) O1s.

Table 5-2. The atomic percentage of all elements present in samples

Sample	C%	N%	O%	Fe2P	Co2p
ZIF8/NPC-900	30.35	0.63	69.02	----	----
Fe/NPC-900	43.51	3.16	53.14	0.19	----
Co/NPC-900	77.26	5.09	17.63	----	0.03
Fe-Co/NPC-900	73.24	6.76	19.83	0.10	0.06

5.2 Electrochemical Performance

The electrochemical performance of the material was evaluated using CV, GCD, and EIS in a 3-electrode system.

5.2.1 Cyclic Voltammetry (CV)

To evaluate the electrochemical characterization of electrode materials (ZIF8/NPC-900, Co/NPC-900, Fe/NPC-900, and Fe-Co/NPC-900), CV, GCD, and EIS measurements were conducted. Specific capacitance was calculated from both CV and GCD measurements using the following relations.

The specific capacitance (F g^{-1}) from CV was calculated using the Equation 1 [7]:

$$C_s = \frac{A}{2m\,\Delta V k} \tag{1}$$

A is the specific area, m is the mass loading, and ΔV is the potential difference.

The specific capacitance (F g^{-1}) From GCD was calculated using the Equation 2 [8]:

$$C_s = \frac{I \times \Delta t}{m \times \Delta V} \tag{2}$$

The I (A) represent the discharge current, Δt (s) is discharge time, ΔV represents the voltage window, and m (g) is the active mass loading of the working electrode. Equations 3 and 4 were used to compute the energy density (E_s, Wh kg^{-1}) and power density (P_s, W kg^{-1}) of the electrode materials using the chronopotentiometry curves [9].

$$E_s = \frac{C_s\,\Delta V^2}{8 \times 3.6} \tag{3}$$

$$P_s = \frac{E}{\Delta t} \quad (4)$$

CV responses of all the samples are shown in Figure 5.6. CV measurements were carried out within the potential window of -0.4 V to 0.2 V at the scan rate of 10, 20, 30, 40, 50, and 100 mV s^{-1}. The estimated C_S values of ZIF8/NPC-900, Fe/NPC-900, Co/NPC-900, and Fe-Co/NPC-900 were 72 F g^{-1}, 225 F g^{-1}, 464 F g^{-1}, and 583 F g^{-1} at 10 mV s^{-1}, respectively as shown in Figure 5.6(e). Due to polarization and low content of nitrogen ZIF8/NPC-900 has very low capacitance as compared to metal doped samples[58]. Fe-Co/NPC-900 exhibited high specific capacitance of 583 F g^{-1}, 528 F g^{-1}, 491 F g^{-1} , 462 F g^{-1}, 439 F g^{-1}, 365 F g^{-1} at 10, 20, 30, 40, 50, and 100 mV s^{-1}, respectively with a well-developed rectangular-shaped CV curves among all samples (Figure 5.6d). Furthermore, with an increment in scan rate from 10 to 100 mV s^{-1}, the corresponding currents of each CV curve improved noticeably, revealing a relatively low resistance of the electrode implying a rapid electrochemical process at the electrode and electrolyte interface [5].

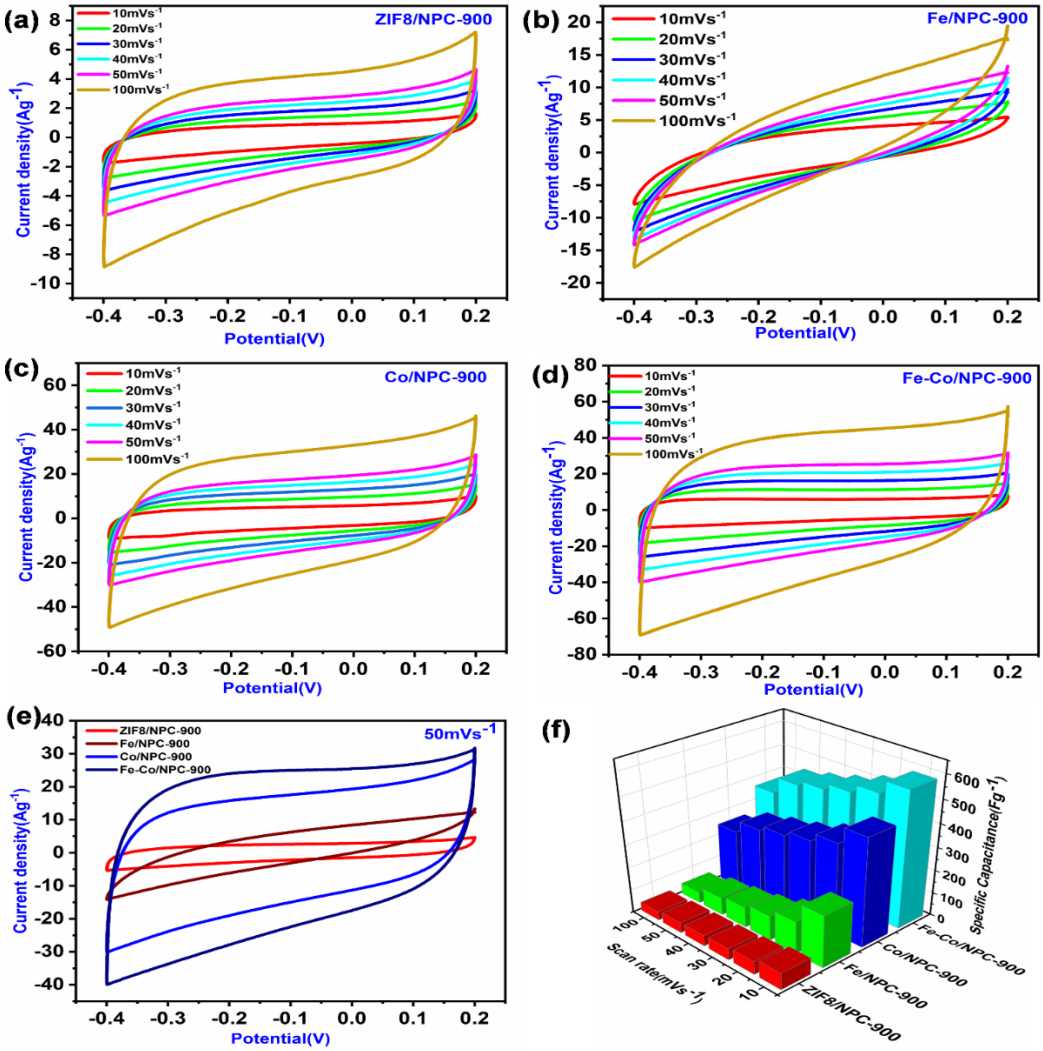

Figure 5-6. CV curves at various scan rates 10–100 mV s^{-1} of (a) ZIF8/NPC-900, (b) Fe/NPC-900, (c) Co/NPC-900, (d) Fe-Co/NPC-900 electrodes, and (e) CV comparison curves of all samples at 50 mV s^{-1}. (f) Calculated specific capacitance of electrodes at different scan rate.

5.2.2 Chronopotentiometry

The GCD curves of all samples at current densities of 5, 10, 15, 20, and 30 A g^{-1} are shown in. GCD curves of all samples showed a reversible triangular shape with equal charge-discharge durations, showing EDLC type charge storage mechanism. Figure 5.7(e) shows the comparison of GCD curves of all the samples at the same current density of 5 A g^{-1}. The specific capacitance exhibited by ZIF8/NPC-900, Fe/NPC-900, Co/NPC-900, and Fe-Co/NPC-900 are 291 F g^{-1}, 358 F g^{-1}, 566 F g^{-1}, and 900 F g^{-1} at 5 A g^{-1} (Figure 5.7e).

With a longer charge/discharge time, Fe-Co/NPC-900 had the highest capacitance and best charge storage capability among all the four samples as shown in . This is due to the appropriate hetero doping of metals which increases the electronic conductivity in porous carbon and resulted in a high surface area (933 $m^2 g^{-1}$) as shown in Table 5.1. The energy densities E_s of ZIF8/NPC-900, Fe/NPC-900, Co/NPC-900, and Fe-Co/NPC-900 calculated using equation 2 were 14.5, 17.9, 28.33, and 45 Wh kg^{-1} at 5 A g^{-1} respectively Table 5.2. Energy density drops with higher current densities because E_s is directly related to C_s, but power density P_s is inversely proportional to discharge duration, which increases with the scan rate and offers less resistance.

Table 5-3. Specific capacitance and energy density of all the synthesized samples at current density 5 Ag^{-1}

Electrode material	Specific capacitance (F g^{-1})	Specific energy (Wh Kg^{-1})
ZIF8/NPC-900	291	14.5
Fe/NPC-900	358	17.91
Co/NPC-900	566	28.33
Fe-Co/NPC-900	900	45

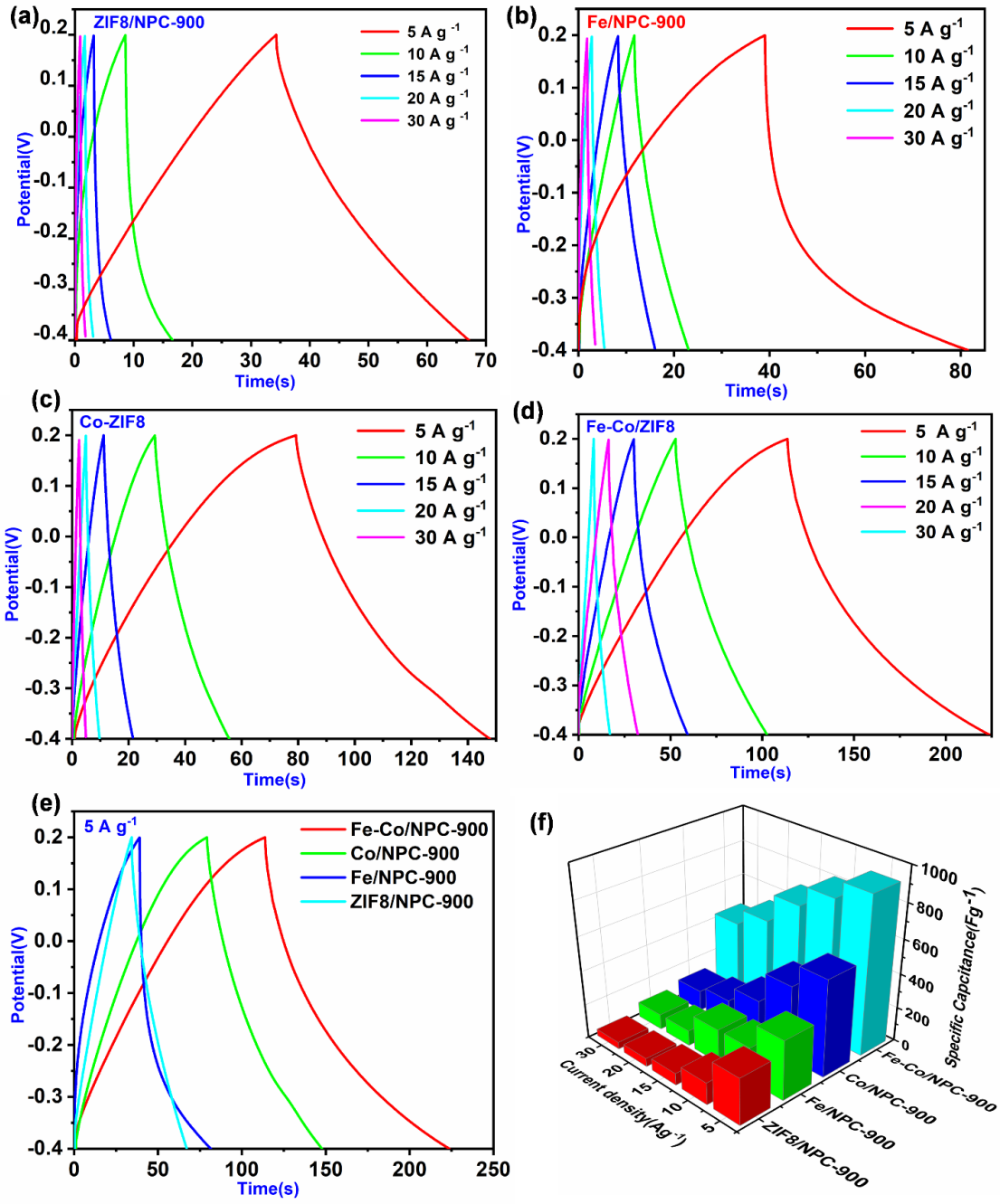

Figure 5-7. GCD curves at current densities of 5–30 A g^{-1} of (a) ZIF8/NPC-900, (b) Fe/NPC-900, (c) Co/NPC-900, and (d) Fe-Co/NPC-900 electrodes. (e) GCD comparison curves of all samples at 5 A g^{-1} and (f) C_s of all electrodes at different current densities.

5.2.3 Capacitive and Diffusive Contribution

An in-depth mathematical analysis was conducted to better understand the material charge storage behavior. The overall specific capacitance of the electrode material can be divided

into two parts based on storage mechanism, i.e., EDLC and diffusion. EDLC comes from the surface adsorption and desorption of ions. It is fast and independent of the scan rate. Diffusion control depends on the diffusion of electrolyte ions into the surface of the electrode material. It is necessary to know which process dominates during an electrochemical reaction to draw conclusions. For a linear scan rate, the current is given by Equation 5.

$$i = av^b \tag{5}$$

Where *i* represents current, *v* represents voltage, and *a* and *b* are constants. The value of *b* is equal to 1 for the EDLC process and 0.5 in the case of diffusion controlled. In most cases, the value of *b* remains between 0.5 and 1. Rearranging Equation 1 as:

$$i(V) = k_1 v + k_2 v^{1/2} \tag{6}$$

Where *i(V)* is the value of the current at a fixed potential. The constants k_1 and k_2 are given by the slope and intercept of a linear regression plot between current and $v^{1/2}$, respectively. It is obvious from Figure 5.8 that the capacitive contribution of bimetallic Fe-Co/NPC-900 is higher than that of ZIF8/NPC-900. The capacitive contribution was calculated at all scan rates for ZIF8/NPC-900 and Fe-Co/NPC-900, which are shown in Fig. 8(b, d) respectively. Capacitive contribution improves with the increase in scan rates. The higher capacitive contribution justifies the good rate capacitance and fast reaction kinetics. These results suggest bimetal combined with nanoporous carbon proves excellent supercapacitor characteristics.

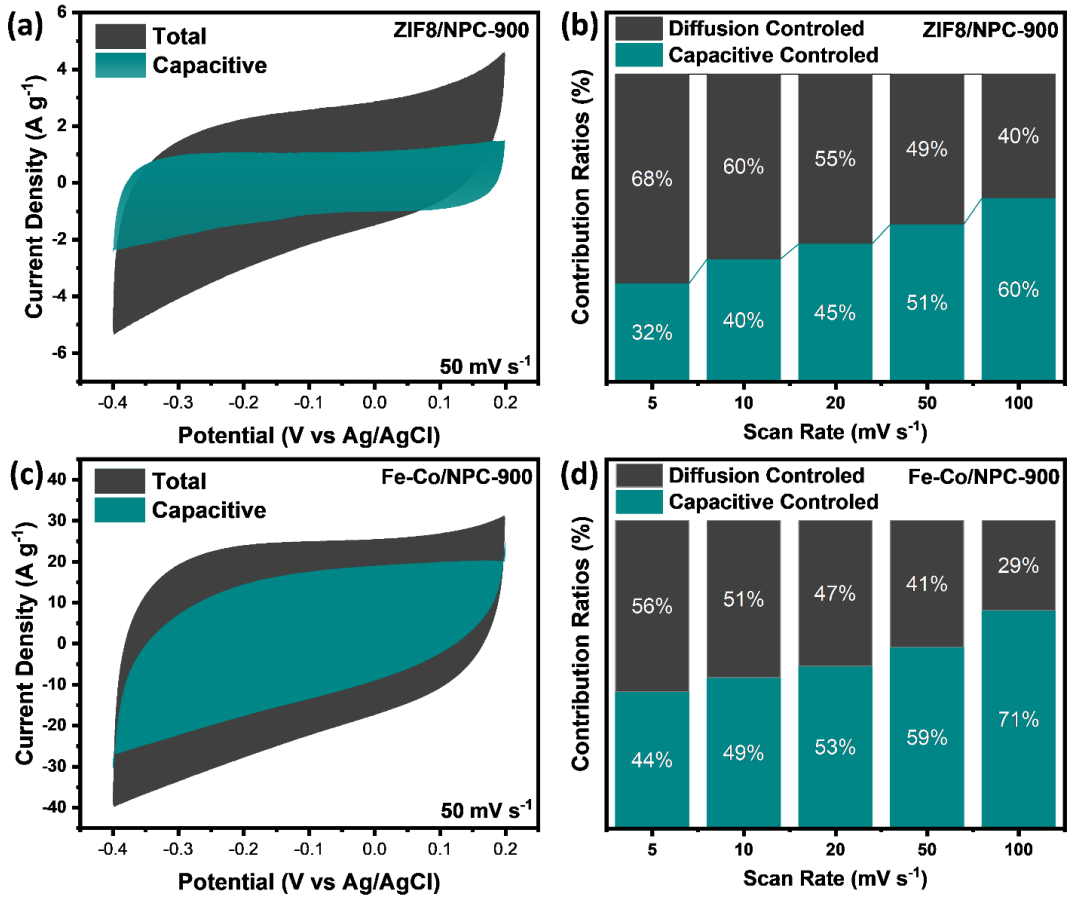

Figure 5-8. Comparison of total current vs capacitive current at 50 mV s^{-1} for (a) ZIF8/NPC-900 and (c) Fe-Co/NPC-900. Surface controlled and diffusion capacitance contribution at different scan rates for (b) ZIF8/NPC-900 (d) Fe-Co/NPC-900.

5.2.4 Cyclic Stability

The Fe-Co/NPC-900's cyclic stability was assessed after 5000 charge-discharge cycles at 30 A g^{-1} and at a potential window of -0.4-2.0 V. Figure 5.9 shows that after such a large number of cycles, 88% of the capacitance was preserved, demonstrating that the Fe-Co/NPC-900 has a longer cyclic life than other electrode materials for supercapacitor applications.

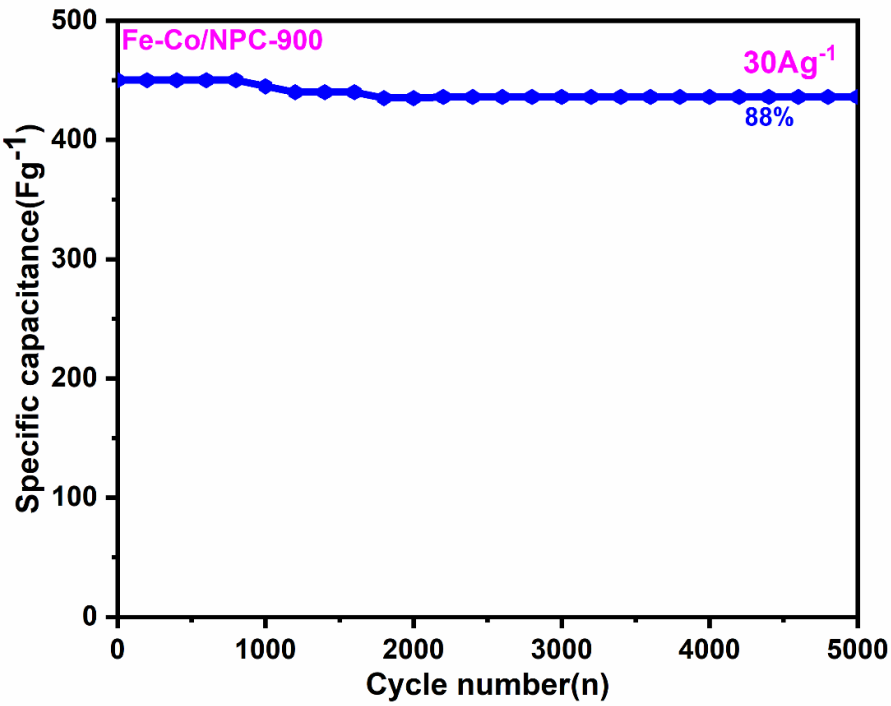

Figure 5-9. Cycle stability of Fe-Co/NPC-900 at 30 A g^{-1} (5000 cycles).

5.2.5 Electrochemical Impedance Spectroscopy

EIS was performed to better understand the capacitive behavior of the samples with respect to electrode resistance. Nyquist curves produced from EIS are illustrated in Figure 5.10 with an equivalent circuit in the inset. The radius of the high frequency region in the Nyquist plot represents the charge transfer resistance (R_{ct}) while the ohmic or solution resistance is represented by offset on the axis of EIS and junction of plot R_{ct} values for ZIF/NPC-900, Fe/NPC-900, Co/NPC-900, and Fe-Co/NPC-900 were around 7.44 Ω, 5.50 Ω, 2.42 Ω, and 1.29 Ω, respectively, calculated from the equivalent circuit of the EIS plots. In comparison to the other electrodes, Fe-Co/NPC-900 has the lowest R_{ct} value, indicating quick charge transfer kinetics and hence improved electron mobility. The EIS plots revealed R_s of 0.45 Ω for Fe-Co/NPC-900, which was lower than 0.63 Ω for ZIF8/NPC-900, 0.51 Ω for Fe/NPC-900, and 0.50 Ω for Co/NPC-900, respectively. The bode plot of prepared samples is shown in Figure 5.10(b). The phase angles of the electrodes were found to agree well with prior findings Figure 5.10(b). ZIF/NPC-900, Fe/NPC-900, Co/NPC-900, and Fe-Co/NPC-900 had phases of 78.5°, 59.1°, 48.5°, and 42.5°, respectively. Because supercapacitor materials have phase angles between 0 and 90 degrees, this verifies the supercapacitor likelihood of electrode materials [10].

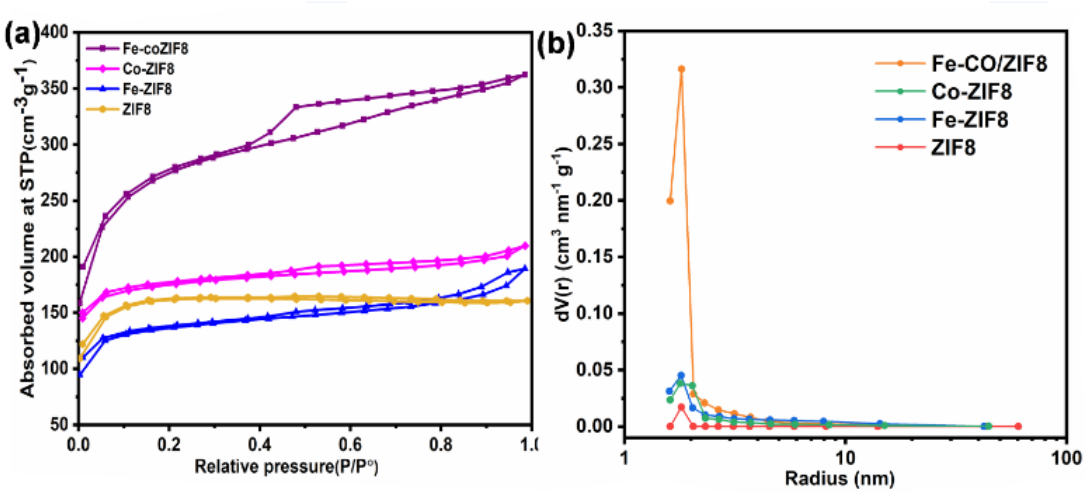

Figure 5-10. (a) Nyquist plot (b) Bode phase angle plot.

Table 5-4. Comparison of similar electrodes specific capacitance from literature

Electrode material	Specific capacitance (F g^{-1})	Current density (A g^{-1})	Ref
Carbon-ZS	285.8	0.1	[11]
ZIF8/NPC900	53.8	0.1	[12]
NPC-750	362	5	[13]
MoP/NPC	544	0.5	[14]
$NiCo_2O_4$@3DNF	1300	1	[15]
Fe-Co/NPC-900	**900**	**5**	**This work**

Summary

All the results obtained during the research are discussed in this chapter. Characterization results of TGA, XRD, SEM, EDS, FTIR, XPS, CV and EIS are supported with facts from previous studies and justified to understand the morphology, structure, composition, thermal stability, functional groups, surface area and porosity of the synthesized materials. Electrochemical results of the synthesized electrodes are discussed at the end. All the results are presented after comparison with the literature and are supported in the light of properties from characterization techniques.

List of references

[1] E. Antolini, "Lithium loss from lithium cobalt oxide: hexagonal Li0.5Co0.5O to cubic Li0.065Co0.935O phase transition," *Int. J. Inorg. Mater.*, vol. 3, no. 7, pp. 721–726, Nov. 2001, doi: 10.1016/S1466-6049(01)00185-4.

[2] B. Leo Brewer and J. Margrave, "Atomic Energy Commission Postdoctoral Fellow," *J. Am. Chem. Soc*, vol. 73, no. 2, p. 10, 1955, Accessed: Jun. 19, 2022. [Online]. Available: https://pubs.acs.org/sharingguidelines.

[3] H. Kimura, M. Asano, and K. Kubo, "Thermochemical study of the vaporization of Li2O(c) by mass spectrometric knudsen effusion method," *J. Nucl. Mater.*, vol. 92, no. 2–3, pp. 221–228, Sep. 1980, doi: 10.1016/0022-3115(80)90106-3.

[4] Y. Meesala *et al.*, "All-Solid-State Li-Ion Battery Using Li1.5Al0.5Ge1.5(PO4)3 As Electrolyte Without Polymer Interfacial Adhesion," *J. Phys. Chem. C*, vol. 122, no. 26, pp. 14383–14389, Jul. 2018, doi: 10.1021/ACS.JPCC.8B03971.

[5] Q. Wang, J. F. Wu, Z. Lu, F. Ciucci, W. K. Pang, and X. Guo, "A New Lithium-Ion Conductor LiTaSiO5: Theoretical Prediction, Materials Synthesis, and Ionic Conductivity," *Adv. Funct. Mater.*, vol. 29, no. 37, p. 1904232, Sep. 2019, doi: 10.1002/ADFM.201904232.

[6] F. Ma *et al.*, "Preparation and evaluation of high lithium ion conductivity Li1.3Al0.3Ti1.7(PO4)3 solid electrolyte obtained using a new solution method," *Solid State Ionics*, vol. 295, pp. 7–12, Nov. 2016, doi: 10.1016/J.SSI.2016.07.010.

[7] A. Manikandan *et al.*, "Rare earth element (REE) lanthanum doped zinc oxide (La: ZnO) nanomaterials: Synthesis structural optical and antibacterial studies," *J. Alloys Compd.*, vol. 723, pp. 1155–1161, Nov. 2017, doi: 10.1016/J.JALLCOM.2017.06.336.

[8] H. Rusdi, N. S. Mohamed, R. H. Y. Subban, and R. Rusdi, "Enhancement of electrical properties of NASICON-type solid electrolytes (LiSn2P3O12) via aluminium substitution," *J. Sci. Adv. Mater. Devices*, vol. 5, no. 3, pp. 368–377, Sep. 2020, doi: 10.1016/J.JSAMD.2020.06.003.

[9] R. O. Fuentes, F. M. Figueiredo, F. M. B. Marques, and J. I. Franco, "Influence of microstructure on the electrical properties of NASICON materials," *Solid State Ionics*, vol. 140, no. 1–2, pp. 173–179, Mar. 2001, doi: 10.1016/S0167-

2738(01)00701-9.

[10] A. Kumar and K. Shahi, “Particle size effect on ionic conductivity in NaCl□Al2O3 composite solid electrolytes,” *Solid State Commun.*, vol. 94, no. 9, pp. 813–816, Jun. 1995, doi: 10.1016/0038-1098(95)00063-1.

[11] G. Yan *et al.*, “Influence of sintering temperature on conductivity and mechanical behavior of the solid electrolyte LATP,” *Ceram. Int.*, vol. 45, no. 12, pp. 14697–14703, Aug. 2019, doi: 10.1016/J.CERAMINT.2019.04.191.

[12] S. Yu *et al.*, “Influence of microstructure and AlPO4 secondary-phase on the ionic conductivity of Li1.3Al0.3Ti1.7 (PO4)3 solid-state electrolyte,” *Funct. Mater. Lett.*, vol. 9, no. 5, Oct. 2016, doi: 10.1142/S1793604716500661.

[13] M. Illbeigi, A. Fazlali, M. Kazazi, and A. H. Mohammadi, “Effect of simultaneous addition of aluminum and chromium on the lithium ionic conductivity of LiGe2(PO4)3 NASICON-type glass–ceramics,” *Solid State Ionics*, vol. 289, pp. 180–187, Jun. 2016, doi: 10.1016/J.SSI.2016.03.012.

[14] D. M. Bykov, G. S. Shekhtman, A. I. Orlova, V. S. Kurazhkovskaya, E. Y. Borovikova, and V. Y. Volgutov, “Multivalent ionic conductivity in the series of phosphates LaxYb1/3 − xZr2(PO4)3 with NASICON structure,” *Solid State Ionics*, vol. 182, no. 1, pp. 47–52, Feb. 2011, doi: 10.1016/J.SSI.2010.11.019.

[15] C. R. Mariappan, G. Govindaraj, S. V. Rathan, and G. V. Prakash, “Preparation, characterization, ac conductivity and permittivity studies on vitreous M4AlCdP3O12 (M = Li, Na, K) system,” *Mater. Sci. Eng. B*, vol. 121, no. 1–2, pp. 2–8, Jul. 2005, doi: 10.1016/J.MSEB.2004.11.005.

Chapter 6: Conclusions and Recommendations

6.1 Conclusions

The current study outlined a method for developing an electrode material for electrochemical energy storage devices. These electrode materials, ZIF8/NPC-900, Fe/NPC-900, Co/NPC-900, and Fe-CO/NPC-900, were synthesized using the co-precipitation technique and pyrolysis. Fe and Co species were successfully doped into Fe-CO/NPC-900. From XPS the existence of Fe^{+2} in Fe-Co/NPC-900 prevented Co/NPC-900 from accumulating, resulting in Fe-Co/NPC-900 with uniform Fe, N, and Co doping, as validated by spectral and analytical techniques. Thermally stable porous Fe-Co/NPC-900 electrode having a high surface area of 933 m^2 g^{-1} demonstrated a high specific capacitance of 900 F g^{-1} at 5 A g^{-1} in an aqueous KOH electrolyte. Fe-Co/NPC-900 electrode produced from bimetal Fe/Co-ZIF8 achieved high capacitance retention of 88% even after 5000 GCD cycles at 30 A g^{-1}, suggesting the electrode's superior stability and potential to use Fe-Co/NPC-900 as electrode material in batteries, sensors, and supercapacitor devices.

6.2 Recommendations

The electrochemical performance and efficiency of supercapacitors for energy storage applications can be increased by exploring new combinations of materials to be employed as electrodes, in addition to the informed selection of electrolytes. The following recommendations are presented to address the shortcomings in the research regarding the electrode materials for supercapacitors:

- Focus of the future research should be towards the various transition metals and their sulfides in addition to the metal oxides to be used as efficient electrode materials for supercapacitors.
- Graphene based materials and composites should be explored to enhance the stretch, flexibility and electrochemical performance of the supercapacitors.

- In contrast to Li-ion batteries, supercapacitors lack the required energy density. Therefore, research is required in the direction of hybrid batteries or hybrid capacitors, i.e., combination of Li-ion and supercapacitor assemblies, to ensure maximum power density and energy density simultaneously.
- MOFs provide the basic framework for such applications, as they demonstrate large surface areas as compared to other compounds and composites. Research should be done to explore the various existing MOFs compounds and their derivatives

Appendix 1- Publications

Fe/Co Doped ZIF Derived Nitrogen Doped Nanoporous Carbon as Electrode Material for Supercapacitors

Ifra Fiaz Gul,[a] Hirra Anwar,[a] Muhammad Arslan Raza,[a] Rabia Ahmed,[a] Naseem Iqbal,[a] Ghulam Ali,[a,*]

Abstract

Nanoporous carbon (NPC) for electrochemical energy storage devices has gained much interest due to its high specific area and tunable porosity. Herein, Fe and Co co-doped NPC is synthesized by a simple co-precipitation method followed by carbonization of Fe and Co doped ZIF8 at 900 °C (Fe-Co/NPC-900). The structural, morphological, elemental, chemical bonding, surface area, and thermal degradation of the synthesized material have been evaluated using X-ray diffraction, scanning electron microscopy, energy dispersive spectroscopy, X-ray photoelectron spectroscopy, Brunauer–Emmett–Teller method, and thermogravimetric analysis, respectively. The high surface area of 933 m^2 g^{-1} and nanoporous structure of Fe-Co/NPC-900 electrode results in a high specific capacitance of 900 F g^{-1} at a current density of 5 A g^{-1}. The cycle performance of Fe-Co/NPC-900 was remarkable with 88% of the capacitance retention after 5000 cycles at a high current density of 30 A g^{-1}. The high electrochemical performance of Fe-Co/NPC-900 is attributed to the hybrid doping of Fe and Co in nitrogen doped carbon network which offers a synergic effect in reaction.

Keywords: Nanoporous carbon; high specific area; co-precipitation; high specific capacitance; synergic effect.

Journal name: **Journal of industrial and Engineering chemistry**

Status : **Accepted**